

Preindustrial to Present day Impact of Changes in Short-lived Pollutant Emissions  
on Atmospheric Composition and Climate Forcing

Vaishali Naik<sup>1\*</sup>, Larry W. Horowitz<sup>2</sup>, Arlene M. Fiore<sup>3</sup>, Paul Ginoux<sup>2</sup>, Jingqiu Mao<sup>4</sup>, Adetutu M.  
Aghedo<sup>5</sup>, and Hiram Levy II<sup>2</sup>

<sup>1</sup> UCAR/NOAA Geophysical Fluid Dynamics Laboratory, Princeton, New Jersey.

<sup>2</sup> NOAA Geophysical Fluid Dynamics Laboratory, Princeton, New Jersey.

<sup>3</sup> Department of Earth and Environmental Sciences and Lamont-Doherty Earth-Observatory,  
Columbia University, Palisades, New York, New York.

<sup>4</sup> Atmospheric and Oceanic Sciences, Princeton University, Princeton, New Jersey.

<sup>5</sup> Civil and Environmental Engineering, Rice University, Houston, Texas.

**\*Corresponding Author:** Vaishali.Naik@noaa.gov

## Abstract

We apply the Geophysical Fluid Dynamics Laboratory chemistry-climate model (GFDL AM3) to assess the changes in atmospheric composition and the net climate forcing resulting from changes in short-lived pollutant emissions (ozone precursors, sulfur dioxide, and carbonaceous aerosols) and methane concentration from preindustrial (1860) to present day (2000). The base AM3 simulation, driven with observed sea surface temperature and sea ice cover over the period 1981-2007, generally reproduces the observed mean magnitude, spatial distribution, and seasonal cycle of tropospheric ozone and carbon monoxide. The global mean aerosol optical depth in our base simulation is within 5% of satellite measurements over the 1982-2006 time period. We conduct a pair of simulations in which only the short-lived pollutant emissions and methane concentrations are changed from pre-industrial to present day levels (i.e., climate, greenhouse gases, and ozone depleting substances held at present-day levels). From the pre-industrial to present-day, we find that the short-lived pollutant emission and methane changes increase the tropospheric ozone burden by 39% and increases the global burdens of sulfate, black carbon and organic carbon by factors of 3, 2.4 and 1.4, respectively. Tropospheric hydroxyl concentration decreases by 7%, showing that increases in OH sinks (methane, carbon monoxide, non-methane volatile organic compounds, and sulfur dioxide) over the last century dominate over sources (ozone and nitrogen oxides) in the model. Combined changes in tropospheric ozone and aerosols cause a net negative top-of-the-atmosphere radiative forcing perturbation ( $-1.05 \text{ Wm}^{-2}$ ) indicating that the negative forcing (direct plus indirect) from aerosol changes dominates over the positive forcing due to ozone increases, thus masking nearly half of the positive forcing [Shindell et al., 2012b] from long-lived greenhouse gases globally.

## 1. Introduction

Although long-lived greenhouse gases in the atmosphere are the dominant contributors to climate change, short-lived climate forcing agents including tropospheric ozone, and sulfate and carbonaceous aerosols have also contributed considerably to the radiative forcing of climate since preindustrial times [Forster et al., 2007]. Controlling emissions of short-lived air pollutants that cause warming, such as tropospheric ozone and black carbon aerosols, has been suggested as a “fast-action” strategy for mitigating climate change [Hansen et al., 2000; Jackson, 2009; Molina et al., 2009; Penner et al., 2010; Shindell et al., 2012a]. Several studies have demonstrated the importance of future evolution of short-lived climate forcers on the climate system [Shindell et al., 2007, 2008; Levy et al., 2008, 2013; Menon et al., 2008; Liao et al., 2009]. Significant progress has been made in quantifying and reducing uncertainties in the preindustrial to present day radiative forcing from individual short-lived climate forcers [Forster et al., 2007; Koch et al., 2009; 2011]. However, the net climate impact from preindustrial to present day changes in short-lived pollutant emissions remains quite uncertain not only because of the uncertainties in their preindustrial emission estimates and atmospheric burden, but also because of their competing radiative effects. For example, increases in tropospheric ozone contribute to climate warming, while the direct impact of increases in black carbon is a warming and that for increases in sulfate and organic carbon is a cooling of the Earth’s climate. Additionally, aerosols affect the radiation budget indirectly by interacting with clouds, resulting in either a warming or cooling [Lohmann and Feichter, 2005; Forster et al., 2007; Koch and Del Genio, 2010; Mahowald et al., 2011]. Our goal here is to quantify the changes in atmospheric composition and the net climate forcing from preindustrial to present day changes in short-lived pollutants using a fully coupled chemistry-climate model.

Short-lived pollutants interact in many ways to influence the atmospheric chemical composition and the Earth's radiation budget [Isaksen et al., 2009]. Changes in emissions of tropospheric ozone precursors, including nitrogen oxides ( $\text{NO}_x$ ), carbon monoxide (CO), methane ( $\text{CH}_4$ ), and non-methane volatile organic compounds (NMVOCs), influence the abundance of tropospheric ozone and its radiative forcing on climate. In addition, they affect the oxidizing capacity of the atmosphere, thereby influencing the lifetime of  $\text{CH}_4$ , itself a near-term climate forcer and an ozone precursor [Fuglestad et al., 1999; Wild et al., 2001; Fiore et al., 2002; Naik et al., 2005; West et al., 2007]. Changes in the oxidant levels (driven by changes in  $\text{O}_3$  and its precursors) can also impact the atmospheric burden of aerosols [Liao et al., 2003; Unger et al., 2006; Bauer et al., 2007]. Changes in aerosol burdens, either induced by chemistry or via direct controls on their (or their precursor) emissions, impact heterogeneous chemistry, modify the atmospheric radiation budget and alter cloud properties, influencing ozone photochemistry [Martin et al., 2003; Bian et al., 2003; Lamarque et al., 2005a; Menon et al., 2008; Unger et al., 2009] and the hydrological cycle [Lohmann and Feichter 2005; Rosenfeld et al., 2008]. Furthermore, anthropogenic emissions of short-lived pollutants are strongly tied to economic development and modulated by air pollution controls. Spatially heterogeneous emissions combined with non-linear chemical interactions result in strong spatial and temporal gradients of short-lived climate forcers and, in turn, an inhomogeneous, highly uncertain climate response.

The recent development of coupled chemistry-climate models has enabled simulations of aerosol-ozone-climate interactions and feedbacks, thus providing an improved understanding of the role of short-lived climate forcers in the climate system. For example, Liao et al. [2009] applied a coupled global atmosphere-tropospheric chemistry-aerosol model with a simplified

ocean module to investigate the impact of future ozone and aerosols on tropospheric composition and climate, while Koch et al. [2011] studied the impact of historical changes in ozone and aerosols using a fully coupled global ocean-atmosphere-aerosol-chemistry model. Although the models of Liao et al. [2009] and Koch et al. [2011] are much advanced from those applied in previous studies (e.g., Levy et al., [2008]), neither considered aerosol indirect radiative effects which could alter their estimates. Here, we improve upon earlier studies by applying the Geophysical Fluid Dynamics Laboratory Atmospheric Model version 3 (GFDL AM3), a fully coupled chemistry-climate model that includes troposphere-stratosphere coupling and aerosol-cloud interactions, to investigate the effects of short-lived pollutants on climate. Specifically, we assess the changes in atmospheric composition and the impact on climate resulting from a change in short-lived pollutants (emissions of  $O_3$  precursors,  $SO_2$ , and carbonaceous aerosols and  $CH_4$  concentration) from preindustrial levels (1860) to present day (2000). In section 2, we describe the key features of the AM3 model and discuss the emissions and boundary conditions implemented in the model. We evaluate the results of a base simulation against observations in section 3. The impact of preindustrial to present day short-lived pollutant emissions on atmospheric composition and climate forcing is presented in section 4. Finally, overall results are discussed and conclusions are drawn in section 5.

## **2. Model Description**

The AM3 model, the atmospheric component of the GFDL coupled model (CM3) [Donner et al., 2011; Griffies et al., 2011], is developed from the GFDL AM2 model [GFDL Global Atmospheric Model Development Team, 2004, hereafter GAMDT04] and has been applied recently to address key questions in chemistry-climate interactions [Fang et al., 2011; Rasmussen et al., 2012; Lin et al., 2012]. In addition to the dynamical and physical updates

described by Donner et al. [2011], the primary new feature of the model is that it simulates tropospheric and stratospheric chemistry interactively (with feed-back to atmospheric radiation) over the full model domain. This unified representation of tropospheric and stratospheric chemistry in AM3 obviates prescribing the concentrations of chemical species important for calculating radiation balance as previously done [GAMDT04, Delworth et al., 2006], thereby removing inconsistencies between the model-generated meteorology and the atmospheric distributions of the forcing agents. The model uses a finite-volume dynamical core on a horizontal domain consisting of, in its standard configuration, 6x48x48 cubed-sphere grid with the grid size varying from 163 km (at the 6 corners of the cubed sphere) to 231 km (near the center of each face), a resolution denoted as C48. The vertical domain of the model extends from the surface up to 0.01 hPa (86 km) with 48 vertical hybrid sigma pressure levels. Chemical species undergo transport (advection, vertical diffusion and convection) in accordance with the AM3 model physics as described by Donner et al. [2011]. An additional key feature of the AM3 model physics is that it simulates aerosol-cloud interactions for liquid clouds [Ming and Ramaswamy, 2009; Golaz et al., 2011] that give rise to the “aerosol indirect effect” – aerosols act as cloud condensation nuclei (CCN) thus increasing cloud albedo (first indirect effect) and increasing cloud lifetime by suppressing precipitation (second indirect effect), and absorbing aerosols can lead to evaporation of clouds (semi-direct effect). Below we describe in detail the chemistry represented in AM3.

## **2.1. Chemistry**

Tropospheric trace gas chemistry in AM3 is based on a modified version of the chemical scheme used in the Model for OZone and Related Tracers version 2 (MOZART-2) [Horowitz et al., 2003, 2007]. It includes reactions of  $\text{NO}_x$ - $\text{HO}_x$ - $\text{O}_x$ - $\text{CO}$ - $\text{CH}_4$  and other NMVOCs. Sulfate

aerosols are produced chemically in the model via the fully coupled gas and aqueous phase oxidation of SO<sub>2</sub> by OH, O<sub>3</sub> and H<sub>2</sub>O<sub>2</sub> and the gas-phase oxidation of dimethyl sulfide (DMS). Organic carbonaceous aerosols are modeled as directly emitted primary organic aerosols (POA) and secondary organic aerosols (SOA) formed by the oxidation of anthropogenic NMVOCs. We include seasonally-varying natural emissions of POA to represent the aerosols produced from the rapid oxidation of biogenic terpenes on the basis of work by Dentener et al. [2006]. In addition, we include a seasonally-varying SOA source of 9.6 Tg C yr<sup>-1</sup> from the oxidation of anthropogenic n-butane calculated offline from previous estimates of butane emissions and monthly OH fields following Tie et al. [2005]. Black carbon and primary organic carbon are converted from hydrophobic to hydrophilic state with an e-folding time of 1.44 days that is within the range of values previously applied in global models [Kanakidou et al., 2005]. Nitrate aerosols are simulated but do not impact radiation calculations in this version of the model. Recent studies estimate that preindustrial to present day changes in nitrate aerosols have contributed only slightly to the aerosol forcing on climate although future reductions in sulfate precursors combined with increases in the emissions of ammonia may lead to a stronger role of nitrate aerosols in the climate system [Bauer et al., 2007; Bellouin et al., 2011]. The size distribution of sea salt and mineral dust aerosols is represented by five size bins each, ranging from 0.1 to 10 μm (dry radius).

Representation of stratospheric chemistry is based on the formulation of Austin and Wilson [2010] that includes the important stratospheric O<sub>3</sub> loss cycles (O<sub>x</sub>, HO<sub>x</sub>, NO<sub>x</sub>, ClO<sub>x</sub>, and BrO<sub>x</sub>), and heterogeneous reactions on sulfate aerosols (liquid ternary solutions) and polar stratospheric clouds (nitric acid trihydrate (NAT) and water-ice). Heterogeneous reactions on liquid ternary solutions are represented based on Carslaw et al. [1995] and those on NAT polar

stratospheric clouds are calculated as in Hanson and Mauresberger [1988]. The rates of change of inorganic chlorine ( $\text{Cl}_y$ ) and inorganic bromine ( $\text{Br}_y$ ) are parameterized as a function of tropospheric concentrations of source gases (CFC11, CFC12,  $\text{CH}_3\text{Cl}$ ,  $\text{CCl}_4$ ,  $\text{CH}_3\text{CCl}_3$ , and HCFC22 for  $\text{Cl}_y$ , and  $\text{CH}_3\text{Br}$ , Halon1211 and Halon1301 for  $\text{Br}_y$ ) for computational efficiency to avoid transporting additional tracers in the model (discussed in detail by Austin et al., 2012). Changes in stratospheric  $\text{O}_3$  and water vapor feed-back to the atmospheric radiation, thereby coupling the climate and chemistry.

The model simulates the atmospheric concentrations of 97 chemical species listed in Table 1 throughout the model domain, of which 16 are aerosol species that are discussed in detail elsewhere [Ginoux et al., in prep]. Here, we focus on the chemistry of 81 species (of which 62 are transported) which undergo 183 gas-phase reactions and 41 photolytic reactions in the model. Kinetic reaction rates are based on JPL 2006 [Sander et al., 2006]. Clear-sky photolysis frequencies are computed using a multivariate interpolation table resulting from calculations using the Tropospheric Ultraviolet and Visible radiation model version 4.4 [Madronich and Flocke, 1998]. Photolysis frequencies are adjusted for simulated overhead stratospheric ozone column, surface albedo, and clouds, but do not account for simulated aerosols. The chemical system is solved numerically using a fully implicit Euler backward method with Newton-Raphson iteration, as in Horowitz et al. [2003]. Changes in tropospheric ozone and aerosols feed-back to atmospheric radiation.

## 2.2. Deposition

Monthly mean dry-deposition velocities are included in the model for gaseous  $\text{O}_3$ , CO,  $\text{CH}_4$ ,  $\text{CH}_2\text{O}$ ,  $\text{CH}_3\text{OOH}$ ,  $\text{H}_2\text{O}_2$ ,  $\text{NO}_2$ ,  $\text{HNO}_3$ , PAN,  $\text{CH}_3\text{COCH}_3$ ,  $\text{CH}_3\text{COOOH}$ ,  $\text{CH}_3\text{CHO}$ ,  $\text{CH}_3\text{COCHO}$ , NO and  $\text{HNO}_4$ . Except for  $\text{O}_3$  and PAN, the deposition velocities are calculated

offline using a resistance-in-series scheme [Wesley, 1989; Hess et al., 2000] as described by Horowitz et al. [2003]. Dry deposition velocities for O<sub>3</sub> are taken from Bey et al. [2001] and those for PAN have been calculated interactively within MOZART version 4 with updates to the resistance-in-series scheme as described by Emmons et al. [2010]. A diurnal cycle is imposed on the monthly mean deposition velocity for O<sub>3</sub> as in Horowitz et al. [2003]. Dry deposition of aerosols includes gravitational settling and impaction at the surface by turbulence.

Wet deposition of soluble gaseous species includes in-cloud and below-cloud scavenging by large-scale (ls) and convective clouds (cv) and are simulated as first-order loss processes. In-cloud scavenging of soluble gases (shown with an asterisk in Table 1) is calculated using the scheme of Giorgi and Chameides [1985]. Below cloud wet scavenging is only considered for large-scale precipitation and is computed for gases following Henry's law as described in Brasseur et al. [1998]. The total rate of wet deposition ( $W$ , in units of mixing ratio s<sup>-1</sup>) for a species is given by,

$$W = (\Gamma_{in}^{cv,ls} + \Gamma_{bc}^{ls}) \cdot C;$$

where,  $C$  (mixing ratio) is the local concentration of the gas,  $\Gamma_{in}^{cv,ls}$  (s<sup>-1</sup>) is the in-cloud scavenging coefficient for large-scale and convective precipitation, and  $\Gamma_{bc}^{ls}$  (s<sup>-1</sup>) is the below-cloud scavenging coefficient for large-scale precipitation. The in-cloud scavenging coefficient for soluble gases is,

$$\Gamma_{in}^{cv,ls} = 1 - e^{(-\beta \cdot f)}; \beta = \frac{P_{rain}^{k+1} - P_{rain}^k + P_{snow}^{k+1} - P_{snow}^k}{\Delta p \cdot g^{-1} \cdot \chi_{liq}},$$

where,  $f$  is the scavenging factor or the fraction of gas incorporated in cloud condensate as determined by the Henry's law equilibrium [Donner et al., 2011],  $P^{k+1} - P^k$  (kg m<sup>-2</sup> s<sup>-1</sup>) is the

precipitation flux generated in layer  $k$ ,  $\Delta p$  (Pa) is the pressure thickness of the model layer  $k$ ,  $g$  ( $\text{m s}^{-2}$ ) is the gravitational acceleration, and  $\chi_{\text{liq}} (= \frac{\text{cloud water (kg)}}{\text{air mass (kg)}})$  is the liquid water content calculated by the large-scale and convective cloud parameterizations. In-cloud wet removal for convective precipitation is computed only within the updraft plumes and mesoscale anvils. In-cloud scavenging is also considered for aerosols following the same scheme but with prescribed values of scavenging factor ( $f$ ) [Donner et al., 2011; Fang et al., 2011].

Below cloud scavenging of gases for large-scale precipitation is computed as

$$\Gamma_{bc}^{ls} = K_g (c_g - c_{g*}),$$

where,  $K_g = \frac{D_g}{d} \left[ 2 + 0.6 \sqrt{\left( \frac{dw_D}{v} \right)^3 \left( \frac{v}{D_g} \right)} \right]$  ( $\text{m s}^{-1}$ ) is the gas-phase mass transfer coefficient,  $c_g$  and  $c_{g*}$  (mixing ratio) are the concentrations of the species in gas-phase and at the surface of the rain drop, respectively, the diffusive coefficient  $D_g = 1.12\text{e-}5 \text{ m}^2 \text{ s}^{-1}$ , the mean diameter of rain drop  $d = 1.89\text{e-}3 \text{ m}$ , the rain drop terminal velocity  $w_D = 7.48 \text{ m s}^{-1}$  and the kinematic viscosity of air  $v = 6.18\text{e-}6 \text{ m}^2 \text{ s}^{-1}$ . Re-evaporation of falling precipitation (where  $P^{k+1} - P^k < 0$ ) returns dissolved species to the atmosphere as in Liu et al. [2001]. Below-cloud washout of aerosols for large-scale precipitation is parameterized as by Fang et al. [2011] and Li et al. [2008].

### 2.3. Emissions and Lower Boundary Conditions

Surface emissions of chemical species are from the new emissions dataset of Lamarque et al. [2010], developed for chemistry-climate model simulations for the Climate Model Inter-comparison Project Phase 5 (CMIP5) in support of the Intergovernmental Panel on Climate Change (IPCC) Fifth Assessment Report (AR5). The inventory provides monthly mean gridded emissions of reactive chemical species, including  $\text{O}_3$  precursors and aerosol species, at a

horizontal resolution of 0.5° latitude x 0.5° longitude for each decade beginning 1850 to 2000. Emissions originating from anthropogenic sources (defined to include energy use in stationary and mobile sources, industrial processes, domestic and agricultural activities), open biomass burning (includes burning of grasslands and forests), ships and aircraft are provided. Surface anthropogenic emissions for the base year 2000 are generated by aggregating existing regional and global emission inventories for 40 world regions and 10 sectors (see Lamarque et al. 2010 for more details). Monthly emissions are given for all sources; however there is no seasonal variation in anthropogenic and ship emissions. Biomass burning emissions for the base year 2000 are from the GFED version 2 inventory [van der Werf et al., 2006]. Since no information on the vertical distribution of these emissions was provided in the original dataset, we followed the recommendations of Dentener et al. [2006] to distribute the biomass burning emissions over six ecosystem-dependent altitude levels between the surface and 6 km. Emissions from agricultural waste burning and fuelwood burning, which are usually specified with biomass burning, are included in anthropogenic residential sector emissions.

The inventory includes ship emissions from international and domestic shipping and fishing, which are based on a recent assessment by Eyring et al. [2009]. As noted by Lamarque et al. [2010], the spatial distribution of ship emissions does not account for dispersion, chemical transformation and sub-grid scale loss processes, which may lead to an over-estimate of ozone formation in global models. The inventory also includes aircraft emissions of nitrogen oxide and black carbon based on calculations using the FAST model [Lee et al., 2005] for the European Quantify project (<http://www.pa.op.dlr.de/quantify/>). Emissions are provided at altitude levels from about 0.3 km to 15 km. As aircraft SO<sub>2</sub> emissions are not provided in the inventory, we

calculate these by scaling the aircraft emissions of BC by an emission ratio of 25 gSO<sub>2</sub>/g BC [Henderson et al., 1999; Hendricks et al., 2004].

Estimates of emissions from natural sources, including plants, soils or oceans, are not provided by Lamarque et al. [2010]. We, therefore, use natural emissions for all relevant gaseous species, including isoprene, from the POET inventory (Precursors of Ozone and their Effects in the Troposphere) for present day (corresponding to year 2000) [Granier et al., 2005; Emmons et al., 2010]. Natural emissions vary from month-to-month, however they do not respond to changes in climate, vegetation or land-use. Soil emissions of NO<sub>x</sub> resulting from agricultural activities are included in anthropogenic sector in the emissions inventory of Lamarque et al. [2010]. Natural soil NO<sub>x</sub> emissions are set to the preindustrial value of 3.6 Tg N yr<sup>-1</sup> following Yienger and Levy [1995] and are assumed to be constant in time. Lightning NO<sub>x</sub> emissions in the model are calculated following Horowitz et al. [2003] as a function of subgrid convection parameterized in AM3 [Donner et al., 2011], resulting in a mean 1981-2000 total source of 4.5 ± 0.2 Tg N (as NO) per year with diurnal, seasonal, and interannual variability based on the model meteorology.

Direct emissions of POA from biological activity in the ocean [O'Dowd et al. 2004] as a function of sea surface temperature and surface winds that vary with climate are also included. DMS emissions are calculated using an empirical function of prescribed fixed monthly mean DMS concentration in sea water and wind speed at 10 m, as described by Chin et al. [2002]. Dust emissions are parameterized following Ginoux et al. [2001] and sea salt particles are emitted from the ocean according to Monahan et al. [1986]. Thus, emissions of oceanic POA and DMS, dust and sea-salt are dependent on the simulated meteorology in the model.

Global total emissions for years 1860 and 2000 are presented in Table 2. Figure 1 shows the global distribution of the absolute change in annual mean surface emissions of NO, CO, NMVOCs, black carbon, organic carbon, and SO<sub>2</sub>, from 1860 to 2000. Although, global mean short-lived pollutant emissions increase from preindustrial to present day (Table 2), emissions for some species from several regions of the world are lower in 2000 (Figure 1). For example, emissions of black carbon and organic carbon from the United States are lower in 2000 compared with 1860, driven by decreases in domestic fuel and biomass burning.

Globally uniform concentrations of well-mixed greenhouse gases (WMGHGs), including, carbon dioxide (CO<sub>2</sub>), nitrous oxide (N<sub>2</sub>O), CH<sub>4</sub>, and ozone depleting substances (ODSs including CFC-11, CFC-12, CFC-113, CCl<sub>4</sub>, CH<sub>3</sub>Cl, CH<sub>3</sub>CCl<sub>3</sub>, HCFC-22) are specified for radiation calculations from the Representative Concentration Pathways database (<http://www.iiasa.ac.at/web-apps/tnt/RcpDb/>) developed for climate model simulations for CMIP5 in support of IPCC-AR5 [Meinshausen et al., 2011]. Global mean concentrations of CH<sub>4</sub> and N<sub>2</sub>O are specified at the surface as lower boundary conditions for chemistry. Tropospheric mixing ratios of halogen source gases are specified for the parameterization of the stratospheric source of Cl<sub>y</sub> and Br<sub>y</sub>.

## **2.4.Simulations**

We perform a base simulation of AM3 for the period 1980-2007 forced with interannually varying observed sea surface temperatures (SST) and sea-ice cover (SIC) [Rayner et al. 2003], following the Atmospheric Model Intercomparison Project (AMIP) configuration. This simulation was forced with time-varying annual mean WMGHG and ODS concentrations, and decadal average short-lived pollutant emissions (with emissions for 1980-2000 from Lamarque et al. [2010] and post 2000 following the Representative Concentration Pathway

(RCP) 4.5 projection from Lamarque et al. [2011]) with interpolation for intermediate years (Table 3). The simulation was run for 28 years with the first year for initial spin-up. We analyze results from this simulation in Section 3 to evaluate the capability of AM3 to simulate the chemical composition of the atmosphere.

We perform two additional simulations of AM3 (Table 3) to investigate the impact of changes in emissions of short-lived species from preindustrial to present levels. These simulations follow the configuration designed by the Atmospheric Chemistry and Climate Model Intercomparison Project (ACCMIP) [Shindell and Lamarque, 2011]. The “2000” simulation uses prescribed climatological monthly mean SST and SIC for the decade 1995-2004 taken from one ensemble member of the 5-member ensemble historical simulation of the GFDL coupled model (GFDL CM3) conducted according to the CMIP5 specifications in support of the IPCC-AR5 [John et al., 2012; Austin et al., 2012]. Concentrations of WMGHGs, including CO<sub>2</sub>, CH<sub>4</sub>, N<sub>2</sub>O, and ODSs, and emissions of short-lived pollutants (non-methane O<sub>3</sub> precursors and aerosols) are set to their year 2000 values. The “1860” simulation uses the same configuration, including the SST and SIC boundary conditions and WMGHG concentrations, except that short-lived pollutant emissions are set to their 1860 values as shown in Table 2 and surface concentrations of CH<sub>4</sub>, a key O<sub>3</sub> precursor [West et al. 2007], are set to their 1860 level (805 ppbv). CH<sub>4</sub> is held at its present day value (1751 ppbv) for radiation calculations in both the 1860 and the 2000 simulation, hence any radiative flux changes between the 2000 and 1860 simulations result from forcing by O<sub>3</sub> and aerosols and not by CH<sub>4</sub>. Since emissions of dust, sea-salt, DMS and oceanic POA depend on simulated meteorology, small differences in their emissions between the present day and preindustrial (Table 1) simulations contribute to their burden changes. Both simulations were run for 11 years with one year for spin-up to obtain a good signal to noise ratio.

We compare results from the 1860 and 2000 simulations in Section 4 to assess the impact of preindustrial to present day changes in short-lived pollutant emissions of and CH<sub>4</sub> burden on atmospheric composition and radiative forcing (only due to changes in O<sub>3</sub> and aerosols). While the configuration with prescribed climatological SST and SIC is computationally efficient as opposed to running the full coupled model, contrasting these simulations provide an estimate of only the fast atmospheric responses but not the slow feedbacks that involve ocean surface temperature changes [Haywood et al., 2009].

### 3. Model Evaluation

We analyze mean results for the 1981-2000 time period from our base simulation, unless noted otherwise. The climate and dynamics simulated in this model integration have been evaluated in detail by Donner et al. [2011].

#### 3.1. Ozone

An annual global tropospheric (defined as the atmospheric domain in which annual mean O<sub>3</sub> concentration is less than 150 ppbv) O<sub>3</sub> burden of 360 Tg is simulated by AM3 (Table 4). The photochemical production and destruction of O<sub>3</sub> are simulated to be 5753 Tg yr<sup>-1</sup> and 5019 Tg yr<sup>-1</sup>, respectively. Net photochemical production of 734 Tg yr<sup>-1</sup> in the troposphere exceeds the stratospheric influx (diagnosed in AM3 as the net dynamical flux) of 450 Tg yr<sup>-1</sup>. Tropospheric loss by dry deposition at the surface accounts for 1205 Tg yr<sup>-1</sup>. The simulated tropospheric O<sub>3</sub> lifetime, calculated as the ratio of O<sub>3</sub> burden and the total loss rate (photochemical loss plus surface deposition) is 21.1 days. Our simulated tropospheric O<sub>3</sub> burden is within 10% of 335 ± 10 Tg derived from observation-based O<sub>3</sub> climatology [Wild, 2007]. A recent inter-comparison of tropospheric ozone budget from 21 global models [Stevenson et al., 2006] estimates the mean

tropospheric O<sub>3</sub> production, loss, dry deposition, stratospheric influx (inferred from the models as the residual of all other budget terms), and lifetime to be  $5110 \pm 606 \text{ Tg yr}^{-1}$ ,  $4668 \pm 727 \text{ Tg yr}^{-1}$ ,  $1003 \pm 200 \text{ Tg yr}^{-1}$ ,  $552 \pm 168 \text{ Tg yr}^{-1}$ , and 22.3 days, respectively, for present day conditions (year 2000), where the range is the multi-model standard deviation. The AM3 tropospheric O<sub>3</sub> budget terms are within the range of these numbers, with the O<sub>3</sub> production, loss and dry deposition at the high end, while AM3 stratospheric flux is at the lower end of the multi-model mean. The global budget of tropospheric ozone simulated by AM3 is within the range of global present day tropospheric ozone budgets from modeling studies post 2000 [Wu et al. 2007] but the AM3 mean tropospheric O<sub>3</sub> burden of 360 Tg is at the high end of the range ( $332 \pm 30 \text{ Tg}$ ) of the more recent Atmospheric Chemistry and Climate Model Intercomparison Project (ACCMIP) [Young et al., 2012].

We evaluate the simulated seasonal cycle of ozone in the lower stratosphere and troposphere by comparison with ozonesonde measurements made between 1995 and 2009. The observations are taken from the climatology described by Tilmes et al. [2012] built on previous work by Logan et al. [1999]. Since the observed data is for 1995-2009, we compare the base simulation averaged over both 1981-2000 and 1995-2007 time periods (Figure 2). With the exception of a few locations, AM3 simulated ozone concentrations are within 10-15 ppbv of the observed values and reproduce the observed seasonal cycle, consistent with results from other chemistry-climate models [Shindell et al., 2006; Lamarque et al., 2012]. We also find little difference in the AM3 O<sub>3</sub> averaged over 1995-2007 versus the baseline time period of 1981-2000 and so we focus our evaluation on the 1995-2007 time period (shown in blue in Figure 2).

At northern high latitude sites (Alert and Resolute), AM3 reproduces much of the seasonal variation in O<sub>3</sub> (correlation coefficient  $r$  calculated using monthly averaged observed

and model data ranges between 0.8 and 0.9) for all vertical levels. The model overestimates the observed  $O_3$  concentrations by 9-13 ppbv in the lower (800 hPa) and middle (500 hPa) troposphere but underestimates observations by 40-50 ppbv in the upper troposphere (200 hPa). This low bias at 200 hPa is consistent with the underestimate of lower stratospheric ozone at northern high-latitudes attributed to a deficiency in model transport (Figure 7 in [Donner et al., 2011]). At northern mid-latitudes (Hohenpeissenberg and Wallops Island), the observed seasonal cycle is represented well at 800 and 200 hPa ( $r > 0.9$ ) but is too weak at 500 hPa. AM3 overestimates  $O_3$  concentrations at these sites by up to 12 ppbv with smaller biases in the mid and upper troposphere. The comparison is similar at southern hemisphere tropical (Samoa) and mid-latitude (Lauder) stations: AM3 represents the  $O_3$  seasonal cycle in the lower and upper troposphere ( $r \sim 0.7-0.9$ ), while misrepresenting it in the mid troposphere (Figure 2). The simulated  $O_3$  concentrations are within 10 ppbv of the observations in much of the southern hemisphere, except AM3 overestimates by 67 ppbv the observations at 200 hPa over Lauder. The high bias in the upper troposphere over southern high-latitudes reflects the overestimate of the observed lower stratospheric  $O_3$  concentrations as indicated by Donner et al. [2011].

We compare the AM3 model zonal mean distribution of tropospheric  $O_3$  concentrations with those measured by the Tropospheric Emission Spectrometer (TES) instrument aboard the NASA-Aura satellite for the period 2005 to 2007 (Figure 3a). We employ the newly released TES version 5 [Herman et al. 2011] for this evaluation. Before calculating the differences between the model and TES, the monthly mean AM3 ozone fields for 2005-2007 were interpolated to TES pressure levels, and TES averaging kernels (AKs) and a priori matrix were then applied to account for differences in vertical resolution and the influence of clouds [Kulawik et al., 2006]. Aghedo et al. [2011] show that applying the monthly mean TES AKs and

a priori profiles to monthly mean model O<sub>3</sub> produces negligible biases compared to convolving the simulated O<sub>3</sub> with TES AKs each day at the overpass time. We find that zonal-mean distribution of AM3 ozone is within  $\pm 4$  ppb (-5% to 10%) for much of the troposphere (surface – 400 hPa) compared with TES observations (Figure 3a). We only show the comparison in the troposphere (i.e. atmospheric domain where O<sub>3</sub> concentration is less than 150 ppbv). In the upper troposphere high latitudes, the bias in the AM3 model ranges from 4–20 ppbv. Note that TES has an equally high bias in this region, due to decreased sensitivity, as found when TES ozone measured in October 2004 to October 2006 were evaluated against ozonesondes [Nassar et al., 2008; Herman et al., 2011]. These results are consistent with the comparison of AM3 with ozonesonde data discussed above.

We further evaluate the AM3 simulated surface O<sub>3</sub> concentrations by comparison with data from surface observational networks in the United States (Clean Air Status and Trends Network – CASTNet <http://www.epa.gov/castnet/>), Europe (European Monitoring and Evaluation Programme – EMEP <http://www.nilu.no/projects/ccc/emepdata.html>), and published data from a few rural sites in India [Naja and Lal, 2002; Naja et al., 2003; Reddy et al., 2008]. O<sub>3</sub> measurements at CASTNet and EMEP sites, located in rural and remote areas with minimal urban influence, are intended to represent background O<sub>3</sub> levels [Tong and Mauzerall, 2006; Reidmiller et al., 2009; Henne et al., 2010], thus making them ideal for evaluating a global model. We obtain climatological monthly means by averaging data over the total observational record at each station: 1988–2009 and 1987–2008 for CASTNet and EMEP, respectively. Based on geographical and topographical characteristics, we divide the U.S. and Europe into six regions and average the data for sites that fall within each region (Table S1). Because of the limited number of observations available from India, we compare the model results with observations at

each of the three individual sites. Surface O<sub>3</sub> observations at Gadanki, Anantapur, and Mt. Abu are for the period 1993-1996 [Naja and Lal, 2002], 2002-2003 [Reddy et al., 2008], and 1993-2000 [Naja et al., 2003], respectively.

AM3 broadly reproduces the observed mean seasonal cycle over all the regions of the United States and Europe ( $r \sim 0.8-0.9$ ) (Figures 4a-l). The model reproduces the observed O<sub>3</sub> concentrations (biases within 3 ppbv) over high-altitude regions in both the United States and Europe (Figures 4c-l), an improvement over the underestimate by chemical-transport models found by Fiore et al. [2009]. At low-altitude sites, AM3 tends to have a high bias compared with observations. In particular, the model overestimates observed surface O<sub>3</sub> concentrations by 15-20 ppbv in the northwest United States and the Mediterranean, where most sites are influenced by maritime air masses resulting in lower O<sub>3</sub> formation suggesting an inadequate representation of chemistry and/or transport in the model. Mean O<sub>3</sub> concentrations biases are within 5 ppbv for Indian sites, except bias exceeds 10 ppbv over Gadanki. AM3 represents the observed seasonal cycle over Anantapur and Gadanki (Figures 4n-o) but misrepresents it over the high-altitude Mt. Abu (Figure 4m). While the model simulates a seasonal cycle at Mt. Abu that is typical of high altitude sites with a spring time maximum due to downward transport from the free troposphere, the observed maximum O<sub>3</sub> concentration in late autumn and winter has been attributed to the influence of cleaner marine airmasses in spring [Naja et al., 2003].

**3.2.** Positive biases in the northern mid-latitudes may be related to a combination of factors including emissions and excessive ozone production in the model, including underestimate of aerosol reactive uptake of HO<sub>2</sub> [Mao et al., 2013], treatment of isoprene nitrates [Horowitz et al., 2007], underestimate of PAN dry deposition [Wu et al., 2012], or omission of halogen chemistry [Parrella et al., 2012]. **Carbon Monoxide**

Next, we evaluate AM3 simulated CO mixing ratios near the surface against observed climatologies for 18 selected stations in the National Oceanic and Atmospheric Administration Environmental Science and Research Laboratory (NOAA ESRL) Carbon Cycle Cooperative Global Air Sampling Network [Novelli and Masarie, 2010]. Monthly mean data over the period 1988-2009 has been used to create a climatology for each station. AM3 is sampled at the grid box and altitude level corresponding to each station (Figure 5). In general, higher CO concentrations are observed in the northern hemisphere than in the southern hemisphere because of higher source strength in the northern hemisphere. The seasonal cycle at northern high and mid-latitudes is strongly a function of photochemistry, with reduced OH abundance and weak vertical mixing resulting in accumulation of CO in the wintertime and increased OH leading to a significant decline in CO concentrations in summer. AM3 underestimates the seasonal variation in CO at all the northern high and mid latitude sites considered here (Figures 5a-f). The discrepancy is largest in late winter and spring when AM3 is biased low by 30-50 ppbv compared with the observations, similar to the multi-model biases discussed by Shindell et al. [2006a]. The negative biases could stem from high OH concentrations (see section 3.3 for a discussion of OH), the neglect of seasonality in anthropogenic CO emissions [Shindell et al., 2006a], or an underestimate of the total source of CO (direct and indirect from VOCs) in AM3.

Observations show lower CO concentrations in the tropics than those at northern high and mid-latitudes because of weaker emissions and more rapid loss. The observed seasonality in the tropics is governed by both anthropogenic and biomass burning emissions, with biomass burning emissions more important close to the equator and in the southern hemisphere tropics [Novelli et al., 1998; Duncan et al., 2007]. AM3 underestimates the seasonality and the magnitude of CO observed at most sites in the northern tropics (Figures 5h-k). The observed

spring time peak CO at Mauna Loa and Mariana Islands is attributed primarily to transport of pollution from Asia [Brasseur et al., 1996; Jaffe et al., 1997]. AM3 does not capture the springtime peak at these stations, indicating a possible problem with model transport and/or the magnitude of anthropogenic emissions from Asia. Mariana Islands is also influenced by dry season (spring) biomass burning in Southeast Asia [Jaffe et al., 1997], where springtime CO concentrations in AM3 are lower than those observed, suggesting a problem with biomass burning emissions. AM3 reproduces the observed spring maximum at Christmas Island but simulates a second peak in fall indicating a problem in the timing of biomass burning emissions. Weakness in the seasonal cycle of biomass burning emissions in AM3 is further highlighted by the early peak (by three months) in simulated CO compared with observations at Ascension Island, a site most sensitive to biomass burning in southern Africa [Novelli et al., 1998]. AM3 captures fairly well the seasonal cycle at subtropical sites in the Southern Hemisphere (Tutuila, Easter Island) sites, but is biased low. In the southern high and mid latitudes where CO concentrations are generally lower and the seasonality is determined by a combination of biomass burning emissions, oceanic emissions, and in-situ hydrocarbon oxidation [Holloway et al., 2000], AM3 reasonably reproduces the observed magnitude and seasonal variation of CO.

We also compare zonal mean AM3 tropospheric CO concentrations for 2005-2007 with those observed by TES (Figure 3b) following the same process of interpolation and application of TES operators (i.e. the TES averaging kernels and a priori matrix) as discussed in Section 3.1. The patterns of global TES CO distributions in the troposphere have been found to agree with those from other satellites (e.g. MOPITT; [Luo et al., 2007a; Ho et al., 2009]). TES CO profiles are also found to be within 10% of averaged in-situ measurements [Luo et al., 2007b; Lopez et al., 2008]. AM3 underestimates the observed CO abundance by up to 20 ppbv in the northern

extra-tropics throughout the troposphere, and by  $\pm 10$  ppbv in the southern troposphere. Elsewhere, the biases are negligible (less than  $\pm 5$  ppbv). These results are also consistent with the comparison with surface CO measurements.

### 3.3. Aerosols

Here, we evaluate AM3 simulated aerosol optical depth (AOD) against those retrieved from satellite measurements. Simulated AOD in our base run has been shown to be somewhat higher than ground-based sun-photometer measurements from the AErosol RObotic NETwork (AERONET), particularly over polluted regions [Donner et al. 2011]. Figure 6 compares the evolution of AOD retrieved from the advanced very high resolution radiometer (AVHRR) over the ocean from 1982-2006 [Geogdzhayev et al., 2002; 2004] with values from AM3. AM3 reproduces the enhancement, though with weaker amplitude, in total AOD after the eruptions of El Chichón (March 1982) and Mount Pinatubo (June 1991), followed by a slow decrease as aerosols are removed from the atmosphere. The mean bias of the AM3 simulated global AOD (tropospheric and stratospheric volcanic aerosols) versus the AVHRR observations is -5% over the 24 years with values ranging from -24% in 1982 to +12 % in 2004. Over the 1996 to 2006 period, when the fraction of volcanic aerosols in the atmosphere is minimal, the mean bias is +2%. The good agreement at the global scale conceals biases on the regional scale as evident from the comparison of regional distribution of AOD from AM3 and AVHRR (bottom panel of Figure 6) for the mean 1996-2006 period. AM3 overestimates the observed AOD in the northern mid-latitude oceans and underestimates in the southern ocean. AM3 also overestimates observed AOD in the tropical and subtropical oceanic regions, particularly those influenced by biomass burning, likely resulting from errors in the biomass burning emissions implemented in the model. Ginoux et al. [2006] have shown that in these regions small bias of simulated relative humidity

introduces large errors in AOD, when relative humidity is in excess of 90%. Detailed evaluation of individual aerosol species concentrations against measurements is addressed by Ginoux et al., [in preparation].

### 3.4. Hydroxyl radical and CH<sub>4</sub> lifetime

Hydroxyl radical (OH) determines the oxidizing capacity of the atmosphere, influencing the lifetime of many short-lived gaseous species [Levy 1971]. The tropospheric OH concentration strongly depends on the atmospheric abundance of O<sub>3</sub>, NO<sub>x</sub>, CO, hydrocarbons, water vapor and the distribution of solar radiation. Primary production of OH occurs when electronically excited O(<sup>1</sup>D) atom, produced by the photolysis of O<sub>3</sub>, combines with water molecules [Levy 1971, Logan et al., 1981, Spivakovsky et al., 2000]. Therefore, OH concentrations are highest in the tropical lower to middle troposphere reflecting high levels of water vapor and ultraviolet radiation. Reaction with CO, CH<sub>4</sub> and NMVOCs, the dominant loss process of OH, produces peroxy radicals (HO<sub>2</sub> or RO<sub>2</sub>) that can regenerate OH via reaction with NO and O<sub>3</sub> [Crutzen, 1973]. This secondary production of OH via radical recycling by NO<sub>x</sub> plays a more important role at higher latitudes where O(<sup>1</sup>D) and water vapor are less abundant [Spivakovsky et al., 2000, Lelieveld, 2002].

Simulated global mean tropospheric OH concentrations can be tested against indirect estimates from observationally constrained budgets of species with known sources and reaction with OH as their primary sink, such as 1, 1, 1-trichloroethane (CH<sub>3</sub>CCl<sub>3</sub>, methyl chloroform), <sup>14</sup>CO, and CHClF<sub>2</sub> (HCFC-22) [Spivakovsky et al., 2000 and references therein]. The lifetime of CH<sub>3</sub>CCl<sub>3</sub> derived from its observed atmospheric abundances and known industrial emissions has most often been used to estimate the global mean abundance of OH [Prinn et al., 1995, 2001;

Krol et al., 1998; Krol and Lelieveld, 2003; Montzka et al., 2000, 2011]. Prinn et al [2001] estimate a global tropospheric mean  $\text{CH}_3\text{CCl}_3$  lifetime of  $5.99^{+0.95}_{-0.71}$  years for the period 1978-2000, while Prather et al. [2012] derive a value of  $6.3 \pm 0.4$  years for 2010. Since AM3 does not simulate the chemistry of  $\text{CH}_3\text{CCl}_3$ , we assume a global uniform atmospheric mixing ratio to calculate its tropospheric lifetime as,  $\tau_{OH} = \frac{1}{\int_{sfc}^{trop} k(T)[OH]}$ , where,  $k(T)$ , the rate constant for the oxidation of  $\text{CH}_3\text{CCl}_3$  by tropospheric OH, is  $1.64 \times 10^{-12} \exp(-1520/T)$  molec<sup>-1</sup> cm<sup>3</sup> s<sup>-1</sup> [Sander et al., 2006]. Our estimated  $\text{CH}_3\text{CCl}_3$  tropospheric mean lifetime of  $5.3 \pm 0.1$  years over the period 1981-2000 is about 11% and 16% lower than the estimates of Prinn et al. [2001] and Prather et al. [2012], respectively; while within the uncertainty range, we conclude that AM3 OH is likely biased high.

AM3 simulates a global mean airmass-weighted OH concentration of  $(1.05 \pm 0.02) \times 10^6$  molecules cm<sup>-3</sup> for the 1981-2000 period, with a northern to southern hemisphere (NH/SH) ratio of 1.16 suggesting that higher concentrations of O<sub>3</sub>, NO<sub>x</sub> and other OH precursors in the northern hemisphere dominate over the higher concentrations of CO, VOCs, and other sinks for OH in the model. While observational constraints on OH (more discussed below) indicate that the annual mean OH concentration is higher in the southern hemisphere than the northern hemisphere (NH/SH < 1) [Prinn et al., 2001; Montzka et al., 2000; Krol and Lelieveld, 2003], most chemistry models [Wang et al., 1998; Dalsøren and Isaksen, 2006; Naik et al., 2012], including AM3, simulate higher northern hemisphere OH concentrations (NH/SH > 1). Krol and Lelieveld [2003] suggest that this discrepancy arises because the mean location of the Intertropical Convergence Zone (ITCZ), at 6°N [Waliser and Gautier, 1993], is used to determine the interhemispheric ratio from observations, implying that the amount of tropical air (with high OH) included in the southern hemisphere is larger than in the northern hemisphere. Models, on the

other hand, assume that the hemispheres are symmetric around the equator. However, the ITCZ is used only in the analysis of Montzka et al. [2000], while Prinn et al. [2001] divides the hemispheres at the equator. Furthermore, observational estimates of NH/SH OH ratio are highly uncertain as they rely on the assumption that the emission estimates and atmospheric observations of  $\text{CH}_3\text{CCl}_3$  are accurate. Nevertheless, high OH concentrations in the northern hemisphere simulated by AM3 reflect the high  $\text{O}_3$  (section 3.1) and low CO biases (section 3.2) there.

We compare the AM3 simulated airmass-weighted annual mean OH concentrations (Figure 7a) with the climatology of Spivakovsky et al. [2000] (Figure 7b) for twelve tropospheric subdomains as recommended by Lawrence et al. [2001]. AM3 simulates the highest boundary layer (surface to 750 hPa) OH burden in the tropics followed by the northern extra-tropics ( $30^\circ\text{N}$ - $90^\circ\text{N}$ ) and the southern extra-tropics ( $30^\circ\text{S}$ - $90^\circ\text{S}$ ), consistent with the climatology (Figure 7b), but is higher by about 25-35%. AM3 OH concentrations decrease with increasing altitude as opposed to first decreasing in the mid-troposphere and then increasing in the upper troposphere as in the Spivakovsky et al [2000] climatology. The vertical OH distribution in AM3 is, however, similar to that of other chemistry-climate models [Folberth et al., 2006; Jöckel et al., 2006; Lamarque et al., 2012]. Excessive OH in the tropical boundary layer could indicate limitations in our treatment of higher volatile organic compounds [Mao et al., 2009]. For example, AM3 does not include representation of higher (5 and more carbon atoms) alkanes, alkenes and aromatic compounds, thus, reducing the OH sink (for example, the MOZART-4 mechanism which includes higher NMVOC yields an OH vertical distribution that better matches the climatology [Emmons et al., 2010]). Furthermore, differences in the AM3 simulated and climatological OH

distributions could also indicate deficiencies in the meteorology simulated by AM3 (e.g., water vapor biases).

AM3 simulates a mean total atmospheric CH<sub>4</sub> burden of 4622 Tg and tropospheric methane loss by reaction with OH of 540 Tg yr<sup>-1</sup>, resulting in mean tropospheric CH<sub>4</sub> lifetime against loss by tropospheric OH of 8.6 years, about 10% lower than the lifetime of 9.6 years reported by Prather et al. [2001]. It is within the range of values (7.8-10.5 years) simulated by other models [Lawrence et al., 2001; Folberth et al., 2006; Jöckel et al. 2006; Fiore et al., 2009; Emmons et al., 2010; Lamarque et al., 2012] and a recent multimodel mean estimate of  $9.7 \pm 1.5$  years [Naik et al., 2012]. Including a nominal stratospheric sink of 40 Tg yr<sup>-1</sup> and a soil sink of 30 Tg yr<sup>-1</sup>, yields a global atmospheric CH<sub>4</sub> lifetime of 7.6 years, on the low side of the  $8.7 \pm 1.3$  and  $8.6 \pm 1.2$  years from multi-model estimates of Stevenson et al. [2006] and Voulgarakis et al. [2012], respectively, and an observation-based estimate of  $9.1 \pm 0.9$  years [Prather et al., 2012].

## **4. Impact of Short-lived pollutants on Composition and Climate**

In this section, we compare 10-year annual mean fields from 2000 and 1860 simulations to investigate the impact of changes in short-lived pollutants (emissions of precursors of ozone and aerosols and CH<sub>4</sub> concentrations) from preindustrial to present levels, on atmospheric composition (Section 4.1) and climate forcing (Section 4.2).

### **4.1. Impact on Atmospheric Composition**

#### **4.1.1. Tropospheric O<sub>3</sub>**

We simulate a 39% increase in the annual mean global tropospheric O<sub>3</sub> burden from 263 Tg in preindustrial to 365 Tg in the present day (Table 4). Of the total 103 Tg increase in tropospheric O<sub>3</sub> burden, 62% occurs in the northern hemisphere, consistent with the much larger

NO<sub>x</sub> emission increase in the northern hemisphere (Figure 1). The photochemical production and loss of ozone increase by 69% and 63%, respectively. The deposition flux of ozone increases by 69% in response to the increased ozone burden. The (photochemical and depositional) lifetime of ozone decreases from 25 days in the preindustrial to 21 days in the present day simulation. In addition, the cross-tropopause flux of ozone is 15% greater in the present day relative to the preindustrial simulation. The global average O<sub>3</sub> column increases by about 16.9 DU with tropospheric and stratospheric increases of 9.4 DU (39%) and 7.5 DU (2%), respectively.

With ODSs held constant at their present day values for both the 2000 and 1860 simulations, the small increase in stratospheric O<sub>3</sub> occurs via changes in CH<sub>4</sub> concentrations. Increasing CH<sub>4</sub> increases water vapor in the upper stratosphere and mesosphere enhancing the loss of O<sub>3</sub> catalyzed by the HO<sub>x</sub> radicals (HO<sub>x</sub> = H + HO<sub>2</sub> + OH). In the lower stratosphere, however, the CH<sub>4</sub> increase causes O<sub>3</sub> to increase via NO<sub>x</sub>-induced O<sub>3</sub> production [Wayne, 1991; Brasseur and Solomon, 1986] just as in the troposphere. Further, increases in CH<sub>4</sub> also act to reduce the chlorine catalyzed destruction of O<sub>3</sub> by converting chlorine atoms to the reservoir hydrochloric acid (HCl; CH<sub>4</sub> + Cl → HCl + CH<sub>3</sub>) in the lower stratosphere [Wayne 1991; Fleming et al., 2011]. Thus, the overall consequence is a slight increase in stratospheric O<sub>3</sub> in the 2000 simulation relative to that in 1860.

Total annual column O<sub>3</sub> is simulated to increase by 25-35 DU over the industrialized areas of the northern hemisphere (Figure 8a). Global annual average surface O<sub>3</sub> concentrations increase by ~14 ppbv from preindustrial to present day, with largest increases over regions coinciding with the largest increases of precursor emissions (Figure 8b). The inter-hemispheric asymmetry (NH/SH) in surface O<sub>3</sub> concentrations increases from 1.1 in preindustrial to 1.4 at present day (the distribution of simulated surface O<sub>3</sub> concentrations for preindustrial and present

day is shown in Figure S1). Greater NO<sub>x</sub> emission increases in the northern hemisphere aided by CH<sub>4</sub> increases (globally uniform) produce more O<sub>3</sub> in the northern hemisphere thus contributing to the enhanced inter-hemispheric asymmetry in surface O<sub>3</sub> in the present day relative to preindustrial.

Our simulated tropospheric O<sub>3</sub> burden increase of 103 Tg in response to changes in short-lived pollutants is within the range (71-140 Tg) of previously published tropospheric ozone increase from preindustrial to present day [Lamarque et al., 2005b and references therein]. It is also within the range of more recent estimates of preindustrial to present day O<sub>3</sub> increases from Liao and Seinfeld [2005] (128 Tg), Horowitz [2006] (113 Tg); Shindell et al. [2006b] (41 Tg), Lamarque et al. [2010] (99 Tg), Skeie et al. [2011] (108 Tg), and Young et al. [2012] (multimodel mean O<sub>3</sub> increase of 88 Tg).

#### **4.1.2. CO and NO<sub>x</sub>**

The global annual mean CO burden increases by 82% from preindustrial to present day (Table 4) in response to changes in the anthropogenic and biomass burning emissions of CO and NMVOC, and CH<sub>4</sub> concentrations. Near-homogenous increases in CO burden are simulated (Figure 8c), except for strong source regions, for example, the biomass burning areas of Southeast Asia, Central Africa, and anthropogenic emissions areas of North America, China and South Asia. Increases in zonal average CO concentrations extend from the surface to the tropopause, with increases of 30 to 60 ppb in the northern hemisphere and 10 to 20 ppb in the southern hemisphere (not shown). Surface CO concentrations increase by up to 400 ppb locally over source regions (Figure 8d).

The annual mean tropospheric NO<sub>x</sub> burden increases by 14% in the present day relative to preindustrial (Table 4), with maximum increases near source regions in the northern hemisphere (Figure 8e). Small decreases in the NO<sub>x</sub> burden in the southern hemisphere are attributed to the simulated decrease in lightning NO<sub>x</sub> emissions over the southern hemisphere extra-tropical land areas (Figure S2). NO<sub>x</sub> emissions from lightning, the main source of NO<sub>x</sub> in the free troposphere, especially in the preindustrial, decrease in the present day by about 6% (Table 4), consistent with a 7% decrease in global lightning frequency (Figure S2). Lightning activity and the resulting NO<sub>x</sub> emissions have generally been understood to increase in a warmer climate [e.g. Price and Rind, 1994; Reeve and Toumi, 1999]. Large uncertainties are associated with the modeling of long-term changes in convection, lightning [Tost et al., 2007; Williams, 2009] and consequently lightning NO<sub>x</sub> emissions [Schumann and Huntrieser, 2007 and references therein]. Aerosols, recently shown to enhance lightning activity and NO<sub>x</sub> emissions [Yuan et al., 2012], add to the complexity of simulating long term changes in lightning NO<sub>x</sub> emissions. Further work is clearly needed to characterize the change in lightning NO<sub>x</sub> emissions from preindustrial to present day.

Annual mean surface NO<sub>x</sub> concentrations increase by up to 3 ppbv over the northeastern US, Europe, northern India and China source regions (Figure 8f), following the preindustrial to present day increases in emissions (Figure 1). Surface NO<sub>x</sub> also increases over oceanic ship tracks, however, this increase may be overestimated as plume processes are not accounted for in our global model [Lamarque et al., 2010]. With a lifetime of a day, most NO<sub>x</sub> increases are confined to near the surface, as opposed to the CO increases that are more homogenous throughout the troposphere.

#### **4.1.3. Aerosols**

Simulated global burdens of sulfate, black carbon and organic carbon increase by factors of three, 2.4 and 1.4 from preindustrial to present day (Table 4), within the range of previous published estimates [Horowitz, 2006; Tsigaridis et al., 2006; Lamarque et al., 2010]. Our simulated global aerosol burden changes are significantly lower than those simulated by Horowitz [2006], in part because of differences in the applied emissions. Horowitz [2006] set preindustrial (1860) anthropogenic emissions of aerosols and their precursors to zero and biomass burning emissions, specifically, those from biofuel, savannah, tropical forest and agricultural waste burning (not extra-tropical forests), to 10% of present day (1990) levels. Thus, Horowitz [2006] apply factors of 75, 12, and 6 increases in the surface emissions of SO<sub>2</sub>, BC, and OC, respectively, in the present day, significantly higher than the factors of 20, 2, and 1.2 applied in this study. Historical emissions of short-lived pollutants are highly uncertain [Lamarque et al., 2010], thus making it difficult to accurately estimate the historical changes in aerosol burden.

The largest increases in sulfate aerosol column occurs in the equator to 30°N latitude band (Figure 8g), a region which is characterized by high emissions and oxidation capacity. The atmospheric burden of sulfate aerosols depends on sources (SO<sub>2</sub> emissions, level of atmospheric oxidants, including O<sub>3</sub>, OH, NO<sub>3</sub><sup>-</sup> and H<sub>2</sub>O<sub>2</sub>) and sinks (wet and dry deposition). Higher present day versus preindustrial SO<sub>2</sub> emissions lead to increased formation of sulfate aerosols in the present day simulation. At the surface, sulfate concentrations increase by up to 15 µg S m<sup>-3</sup> (Figure 8h) in regions of high SO<sub>2</sub> emissions (Asia, Europe, and North America). Secondary maxima in the increase of surface sulfate concentrations occur in the southern hemisphere over regions of high biomass burning (South America, Africa, and Southeast Asia).

The atmospheric burden of carbonaceous aerosols is governed by their emissions and deposition (wet and dry). Black carbon emissions are driven by human activities that involve combustion of mostly fossil fuels with smaller contributions from domestic biofuel burning and biomass burning, while organic carbon emissions predominantly come from the latter two categories. Because of the large natural background source of organic carbon, increase in its global fractional burden is smaller than that for black carbon. Reduced present day emissions from domestic biofuel burning and forest clearing in mid-latitude regions (North America, Europe, and Australia) drive decreases in carbonaceous aerosol burden over these regions (Figures 8i and k). Conversely sharp increases are simulated for regions with high present day emissions (China, India, central Africa). Changes in the burden are dominated by changes near the surface (Figure 8j and l). Simulated present day surface concentrations are lower than preindustrial over most of North America, Europe, and Australia, but exceed preindustrial values in highly populated areas of Asia, Eastern Europe and central Africa (Figures 8j and l).

The global total burdens of dust and sea salt decrease by small amounts (1-2%) in response to their emission reductions in our present day simulation relative to the preindustrial. Since the emissions of these species are dependent on meteorological factors, changes in their burden result from the fast atmospheric responses due to preindustrial to present day changes in short-lived pollutant emissions.

The global mean AOD at 550 nm increases by 50% from a preindustrial value of 0.10 to a present day value 0.15 (Table 4). The largest increase in AOD comes from sulfate, followed by the increase in black carbon and organic carbon, respectively (Figure 9a). Further, the relative contribution of sulfate and black carbon to AOD almost doubles from preindustrial to present day, in response to increases in their atmospheric loading (Table 4). Spatially, the largest

increases in AOD from preindustrial to present day (Figure 9b) coincide with regions of largest increases in anthropogenic emissions (Figure 1). Our estimate of the preindustrial to present day change in AOD is in qualitative agreement with the 21% increase simulated by Tsigaridis et al. [2006].

#### 4.1.4. Tropospheric OH

Next, we investigate the changes in tropospheric oxidizing capacity resulting from preindustrial to present day changes in short-lived pollutant emissions and increases in CH<sub>4</sub> concentration. The tropospheric mean airmass-weighted OH concentration decreases by about 7% (Table 4) in response to preindustrial to present day changes in short-lived pollutants, suggesting that increases in OH sinks (CH<sub>4</sub> burden, and emissions of CO, SO<sub>2</sub>, and NMVOCs) dominate over increases in sources (tropospheric O<sub>3</sub>, water vapor and NO<sub>x</sub> emissions) in the model. The decrease in OH acts to increase the tropospheric lifetime of CH<sub>4</sub> by about 4% (Table 4). When we compare our 2000 simulation with a sensitivity simulation (not shown) in which we set the emissions of NO<sub>x</sub>, CO, NMVOCs and aerosols (or their precursors) to 1860 levels but CH<sub>4</sub> to present day levels, we find that tropospheric mean OH increases by 10% as a result of increasing emissions alone. This suggests that CH<sub>4</sub> plays a dominant role in controlling global mean OH changes over long timescales.

Regionally, OH decreases in all regions of the atmosphere except in the lower (surface to 750 hPa) northern hemisphere, with the largest increase (35%) occurring in the lower extratropical troposphere (Figure 7c), coinciding with the largest increases in OH sources - NO<sub>x</sub> and O<sub>3</sub>. Figure 7d shows the spatial distribution of the increase in OH in the lowest atmospheric subdomain (surface to 750 hPa) where more than 60% of the total oxidation of CH<sub>4</sub> occurs [Lawrence et al., 2001]. OH increases by almost a factor of two over northern hemisphere

regions with high present day  $\text{NO}_x$  emissions and  $\text{O}_3$  concentrations. OH decreases in the southern hemisphere are attributed to increases in  $\text{CH}_4$ , which is more important as an OH sink in the southern than in the northern hemisphere [Spivakovsky et al., 2000].

Large uncertainties exist in the estimates of preindustrial to present day changes in tropospheric OH. Previous modeling estimates of preindustrial to present day changes in tropospheric mean OH abundance range from increases of 6-15% to decreases of 5-33% (see Table 1 of John et al., 2012). Applying transient preindustrial to present day simulations (with time varying WMGHG and ODS concentrations, and short-lived pollutant emissions) of the fully coupled chemistry-climate model, GFDL CM3, John et al. [2012] find a 6% decrease in tropospheric mean OH concentrations. Using results from ACCMIP models, Naik et al. [2012] find that the multi-model mean tropospheric OH abundance has remained nearly constant over the past 150 years. Our estimate of the preindustrial to present day change in OH concentrations falls within the range of these previous estimates.

## **4.2. Impact on Radiative Forcing and Climate**

To investigate the impact of changes in short-lived pollutant emissions from preindustrial to present day on climate, we first assess the net adjusted radiative forcing from these emission changes and then briefly explore the changes in key climate variables. Note that we expect the climate responses to be weak in our experiments, which are conducted with fixed SST and SIC. We calculate the radiative forcing due to combined changes in ozone and aerosols (from emission changes) as the change in the net irradiance (shortwave plus longwave) at the top of the atmosphere (TOA) with fixed ocean conditions, but allowing for rapid adjustments to the climate system (including atmospheric temperatures and clouds). Since our present day and preindustrial simulations use fixed SST and SIC extent, our calculated TOA radiative forcing, more

appropriately referred to as “radiative flux perturbation” (RFP) or fixed-SST forcing, incorporates the effects of fast atmospheric responses to short-lived pollutants but not the slow feedbacks associated with changes in global ocean temperatures [Hansen et al., 2005; Forster et al., 2007; Haywood et al., 2009]. RFP at the TOA has been shown to predict the global mean surface temperature change that will result from changes in short-lived pollutants [Hansen et al., 2005; Forster et al., 2007; Lohmann et al., 2010]. While useful, here we do not diagnose the contribution of individual short-lived climate forcers to the net RFP here. RFPs due to historical changes in individual short-lived climate forcers as simulated by the GFDL AM3 are briefly discussed by Levy et al. [2013] and are fully described by Horowitz et al. [in prep].

The net global annual average all-sky TOA RFP due to ozone and aerosols resulting from preindustrial to present day changes in short-lived pollutant emissions and CH<sub>4</sub> concentrations is -1.05 Wm<sup>-2</sup> in our model, implying a net radiative cooling of the climate system from preindustrial to present day changes in ozone and aerosols. Tropospheric ozone increases produce a positive forcing while aerosol increases exert either a positive forcing (black carbon) or a negative forcing (sulfate, organic carbon) on the climate system. Aerosols also produce a negative indirect forcing via changes in cloud optical properties or a positive forcing from changes in the thermal structure of the atmosphere. Our results indicate that the strong negative forcing (direct plus indirect) from preindustrial to present day aerosol changes dominates over the positive forcing due to O<sub>3</sub> increases and aerosol semi-direct effect. Our net ozone and aerosol RFP of -1.05 Wm<sup>-2</sup> is comparable to the multi-model mean (8 models) preindustrial to present day aerosol plus ozone forcing of  $-0.84 \pm 0.50$  Wm<sup>-2</sup> (from Table 10 of Shindell et al., 2012b). Further, our net ozone and aerosol RFP offsets nearly half of the positive radiative forcing of  $2.30 \pm 0.23$  Wm<sup>-2</sup> from preindustrial to present day changes in WMGHGs calculated by Shindell

et al. [2012b], indicating that on a global scale, short-lived pollutants have acted to mask a portion of the anthropogenic greenhouse gas forcing. Thus, future reductions in short-lived pollutant emissions for health reasons will likely unmask the warming due to long-lived greenhouse gases [Levy et al., 2013].

Figure 10a shows the geographical distribution of the annual mean all-sky TOA RFP due to preindustrial to present day short-lived pollutant emissions. The largest statistically significant negative RFPs (up to  $-10 \text{ Wm}^{-2}$ ) are simulated over industrialized regions of northern hemisphere characterized by high aerosol burdens (China, India, Europe, North America). Smaller negative RFPs are also simulated for regions where biomass burning emissions increased over the last century, such as, south-east Asia, central Africa, and parts of the Amazon, and over oceans downwind of source regions. The simulated forcing over much of the globe is statistically insignificant relative to the model internal variability, possibly because 10 year runs are too short to produce a robust signal that can be distinguished from noise [Golaz et al., 2011].

To explore the role of changes in cloud properties on radiative forcing, we break-down the all-sky RFP to clear-sky and cloudy-sky components. Clear-sky radiative fluxes (shortwave and longwave) are calculated by diagnostic calls to the radiation code in the model including the aerosol absorption and scattering but excluding cloud absorption and scattering, thus these fluxes do not include changes from aerosol indirect effects and cloud modifications via direct aerosol interactions [Golaz et al., 2011]. We diagnose the cloudy-sky RFP (includes aerosol indirect effects and cloud modifications via direct aerosol interactions) by taking the difference between all- and clear-sky RFP. Figures 10b and 10c show the spatial distribution of the clear-sky and cloudy-sky RFPs. From a global mean perspective, both the clear and cloudy sky RFP are negative and the contribution of the cloudy sky RFP ( $-0.65 \text{ Wm}^{-2}$ ) is slightly higher than that of

clear-sky RFP ( $-0.40 \text{ Wm}^{-2}$ ) to the all-sky RFP, suggesting that aerosol indirect effects and direct cloud modifications contribute strongly to the net ozone plus aerosol forcing. Spatially, negative RFPs over and downwind of industrialized areas in the northern hemisphere, and biomass burning regions persist in the clear-sky component (Figure 10b), suggesting the dominance of reflecting aerosols (sulfate and organic) over absorbing aerosols (black carbon) and tropospheric ozone.

Next, we analyze the RFP at the surface, as observational evidence indicates that aerosols affect the surface energy budget and hydrological cycle [Ruckstuhl et al., 2008; Philipona et al., 2009]. Preindustrial to present day change in short-lived pollutant emissions results in a global mean all-sky surface RFP of  $-2.5 \text{ Wm}^{-2}$ , implying that the emission changes result in an additional  $1.5 \text{ Wm}^{-2}$  absorbed by the atmosphere. The geographical distribution of all-sky surface RFP (Figure 11a) is similar to that of the TOA RFP but with enhanced negative forcing (up to  $-20 \text{ Wm}^{-2}$ ) over industrialized regions and biomass burning area characterized by large aerosol burden changes, and neighboring oceans. The clear-sky component of the surface RFP (Figure 11b) dominates over the cloudy sky component (Figure 11c). Previous studies have indicated that aerosols have a stronger impact on precipitation than well-mixed greenhouse gases because the former can effectively alter the surface shortwave flux available for evaporation [Feichter et al., 2004; Lohmann and Feichter 2005; Ming and Ramaswamy, 2009]. Consistent with the negative surface forcing, we find that the global mean precipitation diminishes by  $0.03 \text{ mm yr}^{-1}$ , however, much of the spatial distribution of the precipitation change is statistically insignificant (see supplementary Figure S3b).

We also assess the changes in the global mean and spatial distribution of surface air temperature, precipitation and cloud cover in response to preindustrial to present day changes in

short-lived pollutant emissions. Relative to preindustrial, the present day global mean surface air temperature is simulated to decrease by only 0.05 K. Examining the spatial distribution of surface temperature change reveals that it is significant at 95% level (using student's t-test) only over ~5% of the total global land area (Figure S3a), failing a field significance test. Our simulated temperature change, including only the effects of rapid atmospheric adjustments to the applied forcing, is much less than would occur if we had not kept the SSTs constant and allowed the ocean to respond to short-lived pollutant perturbations [Hansen et al., 2005]. On a global scale, cloud cover increases by 0.2%, but the change is found to be statistically insignificant over much of the globe (Figure S3c).

## 5. Discussion and Conclusions

In this study, we have evaluated our base GFDL AM3 simulation (1980-2007 with interannually varying SSTs and SIC) against observations of key chemical species (Section 3) and have employed the model to investigate the net impact of short-lived air pollutant emission changes from preindustrial to present day on atmospheric composition and climate forcing (Section 4). Comparison of our base simulation with observations suggests that AM3 is able to reproduce the observed tropospheric ozone ( $O_3$ ) seasonal cycle (pearson correlation coefficient  $r=0.45-0.97$ ) and simulated concentrations are within 10 to 15 ppbv of observed values. Surface carbon monoxide (CO) concentrations are biased low in late winter and spring compared with observations at all northern high and mid-latitude sites similar to the multi-model biases discussed in Shindell et al. [2006a], but the observed seasonality ( $r=0.91-0.96$ ) and magnitude is captured at southern hemisphere mid and high latitudes. Tropospheric CO concentrations for 2005-2007 in our base simulation are within 15% of those observed by the TES satellite. Global mean aerosol optical depth agrees well with that observed by the AVHRR satellite over the

1982-2006 time period, however there are regional differences of opposite signs. Hydroxyl radical (OH), the primary determinant of the tropospheric lifetime of many short-lived pollutants, is somewhat higher in our base simulation than in the climatological estimates, consistent with the high O<sub>3</sub> and low CO biases in our model. Consistent with high OH, our mean tropospheric methane (CH<sub>4</sub>) lifetime is 8.6 years, on the lower side of published values.

Contrasting the atmospheric composition in our preindustrial (1860) and present day (2000) simulations, both with fixed present day sea-surface temperature, sea-ice extent, and WMGHG concentrations, shows substantial increases in the present day global total burdens of tropospheric ozone, sulfate and carbonaceous aerosols relative to preindustrial driven by short-lived pollutant emission and CH<sub>4</sub> concentration changes. Spatially, surface ozone increases everywhere, more so in the northern hemisphere than in the southern hemisphere, mostly driven by increases in NO<sub>x</sub> emissions. Spatially inhomogeneous changes in aerosol burdens result from the different regional trends in their emissions. For example, carbonaceous aerosol burdens over North America and Europe decrease from the preindustrial to the present day because of reduced domestic fuel burning. Uncertainties in short-lived pollutant emissions will influence our estimate of the historical changes in the abundance of ozone and aerosols. Lamarque et al. [2010] note that uncertainties in regional emissions can be larger than a factor of 2.

We simulate a 7% decrease in tropospheric air-mass-weighted OH concentration for present day relative to preindustrial, indicating that increases in sinks (CH<sub>4</sub>, CO, NMVOCs, and SO<sub>2</sub>) dominate over sources (O<sub>3</sub> and NO<sub>x</sub>) of OH. Consequently, a 6% reduction in CH<sub>4</sub> lifetime is simulated for the present day relative to preindustrial. Analysis of our fully coupled climate-chemistry atmosphere-ocean model (GFDL CM3) simulations with short-lived pollutant emissions and greenhouse gas concentrations, including CH<sub>4</sub>, evolving over the entire historical

period shows that CH<sub>4</sub> lifetime increases from preindustrial to present day, demonstrating the dominant impact of CH<sub>4</sub> on its own lifetime [John et al., 2012]. Although we consider the direct influence of aerosols on gases via heterogeneous chemistry, we do not include their impact on photolysis rates, previously shown to increase the CH<sub>4</sub> lifetime by decreasing tropospheric OH [Bian et al., 2003]. In addition, we did not consider stratospheric ozone depletion resulting from preindustrial to present day increases in ODSs, which could modulate the changes in tropospheric ozone and aerosol burden, oxidizing capacity and therefore CH<sub>4</sub> lifetime. The impacts from historical changes in ODS should be considered to estimate more completely the full anthropogenic influence on the chemistry-climate system over the last century.

We analyze radiative forcing at the top-of-the-atmosphere (TOA), expressed as radiative flux perturbation, to estimate that substantial anthropogenic increases in tropospheric ozone and aerosols burden in the present day relative to preindustrial cause a strong negative forcing (-1.05 Wm<sup>-2</sup>). This finding suggests that the negative forcing (direct plus indirect) from aerosol changes dominates over the positive forcing due to O<sub>3</sub> increases and aerosol semi-direct effect, thus masking nearly half of the historical long-lived greenhouse gas forcing globally. Statistically significant negative TOA forcing is concentrated over industrialized regions of the northern hemisphere characterized by high sulfate aerosol burden changes (China, India, Europe, and North America). Negative forcing is enhanced at the surface and is more widespread compared with the TOA forcing. Our estimate of the TOA forcing from short-lived pollutants may be compared with other estimates obtained using the CMIP5 emissions inventory applied here. For example, Bauer et al. [2012] used this inventory to calculate a TOA forcing of -0.6 Wm<sup>-2</sup> for preindustrial to present day changes in aerosol (or aerosol precursor) emissions only. Our stronger negative TOA forcing compared with that of Bauer et al. [2012] could be attributed to

differences in model configuration (their model included only the cloud albedo effect of aerosols). Similar experiments with other chemistry-climate models will help to determine whether this net impact of short-lived pollutants on climate since the preindustrial period is robust.

We simulate a global annual mean cooling of 0.05 K at the surface from historical changes in short-lived pollutant emissions. However, this change in surface air temperature is statistically insignificant and understates the true change that would result from changes in short-lived pollutants, because we keep the sea-surface temperature and sea-ice extent fixed for both the preindustrial and present day simulations, allowing only rapid atmospheric adjustments – a major limitation of our study. Changes in the total cloud cover and precipitation are statistically insignificant over most of the globe, indicating that 10 year simulations are too short to produce a robust signal that can be distinguished from noise. Analysis of simulations of the GFDL CM3 model with evolving sea-surface temperature and sea ice extent is currently underway to fully assess the impact of short-lived pollutants on climate [Horowitz et al. in prep, Levy et al., 2013].

## **6. Acknowledgments**

We are grateful to Simone Tilmes and Martin Schultz for kindly providing ozonesonde data and surface ozone analysis package, respectively. We thank Yuanyuan Fang, Issac Held, Jasmin John, Meiyun Lin, Yi Ming, and V. Ramaswamy for useful discussions. We appreciate helpful comments and suggestions from Songmiao Fan on an earlier version of this manuscript. Comments from three anonymous reviewers also helped to improve this manuscript.

## **7. References**

896 Aghedo, A. M., K. W. Bowman, D. T. Shindell, and G. Faluvegi (2011), The impact of orbital  
897 sampling, monthly averaging and vertical resolution on climate chemistry model  
898 evaluation with satellite observations, *Atmos. Chem. Phys.*, 11, 6493–6514.

899 Austin, J., and J. Wilson (2010), Sensitivity of polar ozone to sea surface temperatures and  
900 halogen amounts, *J. Geophys. Res.*, 115, D18303, doi:10.1029/2009JD013292.

901 Austin, J., L. W. Horowitz, M. D. Schwarzkopf, R. J. Wilson, and H. Levy II (2012),  
902 Stratospheric ozone and temperature simulated from the preindustrial era to present day,  
903 *J. Climate.*, 10.1175/JCLI-D-12-00162.1, in press.

904 Bauer, S. E., D. Koch, N. Unger, S. M. Metzger, D. T. Shindell, and D. G. Streets (2007), Nitrate  
905 aerosols today and in 2030: a global simulation including aerosols and tropospheric  
906 ozone, *Atmos. Chem. Phys.*, 7, 5043-5059, doi:10.5194/acp-7-5043-2007.

907 Bauer, S. E., and S. Menon (2012), Aerosol direct, indirect, semidirect, and surface albedo  
908 effects from sector contributions based on the IPCC AR5 emissions for preindustrial and  
909 present-day conditions, *J. Geophys. Res.*, 117, D01206, doi:10.1029/2011JD016816.

910 Bellouin, N., J. Rae, A. Jones, C. Johnson, J. Haywood, and O. Boucher (2011), Aerosol forcing  
911 in the Climate Model Intercomparison Project (CMIP5) simulations by HadGEM2-ES  
912 and the role of ammonium nitrate, *J. Geophys. Res.*, 116, D20206,  
913 doi:10.1029/2011JD016074.

914 Bey I., D. J. Jacob, R. M. Yantosca, J. A. Logan, B. Field, A. M. Fiore, Q. Li, H. Liu, L. J.  
915 Mickley, and M. Schultz (2001), Global modeling of tropospheric chemistry with

916 assimilated meteorology: Model description and evaluation, J. Geophys. Res., 106,  
 917 23,073-23,096.

918 Bian, H. and M. Prather (2003), Tropospheric aerosol impacts on trace gas budgets through  
 919 photolysis, J. Geophys. Res., 108(D8), 4242, doi:10.1029/2002JD002743.

920 Brasseur, G. P., D. A. Hauglustaine, and S. Walters (1996), Chemical compounds in the remote  
 921 Pacific troposphere: comparison between MLOPEX measurements and chemical  
 922 transport model calculations, J. Geophys. Res., 101, 14,795-14,813.

923 Brasseur, G. P., et al. (1998), MOZART, a global chemical transport model for ozone and related  
 924 tracers: 1. Model description, J. Geophys. Res., 103, 28265-28289.

925 Brasseur, G. P. and S. Solomon (1986), Aeronomy of the Middle Atmosphere, Second Edition,  
 926 Dordrecht, The Netherlands, 644pp.

927 Carslaw, K. S., B. P. Luo, and T. Peter (1995), An analytic expression for the composition of  
 928 aqueous  $\text{HNO}_3\text{-H}_2\text{SO}_4$  stratospheric aerosols including gas phase removal of  $\text{HNO}_3$ ,  
 929 Geophys. Res. Lett., 22, doi: 10.1029/95GL01668, 1877-1880.

930 Chin, M., P. Ginoux, S. Kinne, O. Torres, B. N. Holben, D. N. Duncan, R. V. Martin, J. A.  
 931 Logan, A. Higurashi, and T. Nakajima (2002), Tropospheric aerosol optical depth from  
 932 the GOCART model and comparisons with satellite and Sun photometer measurements,  
 933 J. Atmos. Sci., 59, 461– 483.

934 Crutzen, P.J. (1973), A discussion of the chemistry of some minor constituents in the  
 935 stratosphere and troposphere, Pure Appl. Geophys., 106-108, 1385-1399.

936 Dalsøren, S. B. and I. S. A. Isaksen (2006), CTM study of changes in tropospheric hydroxyl  
 937 distribution 1990–2001 and its impact on methane, *Geophys. Res. Lett.*, 33, L23811,  
 938 doi:10.1029/2006GL027295.

939 Delworth, T. L., et al. (2006), GFDL's CM2 Global Coupled Climate Models. Part I:  
 940 Formulation and Simulation Characteristics, *Journal of Climate*, 19(5),  
 941 doi:10.1175/JCLI3629.1.

942 Dentener, F., S. Kinne, T. Bond, O. Boucher, J. Cofala, S. Generoso, P. Ginoux, S. Gong, J. J.  
 943 Hoelzemann, A. Ito, L. Marelli, J. E. Penner, J.-P. Putaud, C. Textor, M. Schulz, G. R.  
 944 van der Werf, and J. Wilson (2006), Emissions of primary aerosol and precursor gases in  
 945 the years 2000 and 1750 prescribed datasets for AeroCom, *Atmos. Chem. Phys.*, 6, 4321-  
 946 4344.

947 Donner et al. (2011), The dynamical core, physical parameterizations, and basic simulation  
 948 characteristics of the atmospheric component of the GFDL global coupled model CM3, *J.*  
 949 *Climate*, 24, 3484–3519, doi: /dx.doi.org/10.1175/2011JCLI3955.

950 Duncan, B., J. A. Logan, I. Bey, I. A. Megretskaya, R. M. Yantosca, P. C. Novelli, N. B. Jones,  
 951 and C. P. Rinsland (2007), Global budget of CO, 1988-1997: Source estimates and  
 952 validation with a global model, *J. Geophys. Res.*, 112, D22301,  
 953 doi:10.1029/2007JD008459.

954 Emmons, L. K., S. Walters, P. G. Hess, J.-F. Lamarque, G. G. Pfister, D. Fillmore, C. Granier,  
 955 A. Guenther, D. Kinnison, T. Laepple, J. Orlando, X. Tie, G. Tyndall, C. Wiedinmyer, S.  
 956 L. Baughcum, and S. Kloster (2010), Description and evaluation of the Model for Ozone  
 957 and related chemical Tracers, version 4 (MOZART-4), *Geosci. Model Dev.*, 3, 43-67.

958 Eyring, V., I. S. A., Isaksen, T. Berntsen, W. J. Collins, J. J. Corbett, O. Endresen, R. G.,  
 959 Grainger, J. Moldanova, H. Schlager, and D. S. Stevenson (2009), Transport impacts on  
 960 atmosphere and climate: Shipping, Atmos. Environ.,  
 961 doi:10.1026/j.atmosenv.2009.04.059.

962 Fang, Y., A. M. Fiore, L. W. Horowitz, A. Gnanadesikan, I. Held, G. Chen, G. Vecchi, and H.  
 963 Levy (2011), The impacts of changing transport and precipitation on pollutant  
 964 distributions in a future climate, J. Geophys. Res., 116, D18303,  
 965 doi:10.1029/2011JD015642.

966 Feichter, J., E. Roeckner, U. Lohmann, and B. Leipert (2004), Nonlinear aspects of the climate  
 967 response to greenhouse gas and aerosol forcing, J. Clim., 17, 2384-2398.

968 Fiore, A. M., D. J. Jacob, B. D. Field, D. G. Streets, S. D. Fernandes, and C. Jang (2002),  
 969 Linking air pollution and climate change: The case for controlling methane, Geophys.  
 970 Res. Lett., 29(19), 1919, doi:10.1029/2002GL015601.

971 Fiore, A. M., et al. (2009), Multimodel estimates of intercontinental source-receptor relationships  
 972 for ozone pollution, J. Geophys. Res., 114, D04301, doi:10.1029/2008JD010816.

973 Fleming, E. L., C. H. Jackman, R. S. Stolarki, and A. R. Douglass (2011), A model study of the  
 974 impact of source gas changes on the stratosphere for 1850-2100, Atmos. Chem. Phys., 11,  
 975 8515-8541.

976 Folberth, G. A., D. A. Hauglustaine, J. Lathière, and F. Brocheton (2006), Interactive chemistry  
 977 in the Laboratoire de Météorologie Dynamique general circulation model: model

978 description and impact analysis of biogenic hydrocarbons on tropospheric chemistry,  
 979 Atmos. Chem. Phys., 6, 2273-2319.

980 Forster, P., et al. (2007), Changes in atmospheric constituents and in radiative forcing, in Climate  
 981 Change 2007: The Physical Science Basis. Contribution of Working Group I to the  
 982 Fourth Assessment Report of the Intergovernmental Panel on Climate Change, edited by  
 983 S. Solomon et al., pp. 129–234, Cambridge Univ. Press, Cambridge, U. K.

984 Fuglestvedt, J. S., T. K. Berntsen, I. S. A. Isaksen, H. Mao, X.-Z. Liang, and W.-C. Wang  
 985 (1999), Climatic forcing of nitrogen oxides through the changes in tropospheric ozone  
 986 and methane; global 3D model studies, Atmos. Environ., 33, 961-977.

987 Geogdzhayev, I. V., M. I. Mishchenko, W. B. Rossow, B. Cairns, and A. A. Lacis (2002), Global  
 988 two-channel AVHRR retrievals of aerosol properties over the ocean for the period of  
 989 NOAA-9 observations and preliminary retrievals using NOAA-7 and NOAA-11 data, J.  
 990 Atmos. Sci., 59, 262– 278.

991 Geogdzhayev, I. V., M. I. Mishchenko, L. Liu, and L. Remer (2004), Global two-channel  
 992 AVHRR aerosol climatology: Effects of stratospheric aerosols and preliminary  
 993 comparisons with MODIS and MISR retrievals, J. Quant. Spectrosc. Radiat. Transfer,  
 994 88, 47– 59.

995 GFDL Global Atmospheric Model Development Team (2004), The new GFDL global  
 996 atmosphere and land model AM2-LM2: evaluation with prescribed SST simulations, J.  
 997 Clim, 17, 4641-4673.

998 Giorgi, F., and W. L. Chameides (1985), The rainout parameterization in a photochemical model,  
 999 J. Geophys. Res., 90, 7872–7880.

1000 Ginoux, P., M. Chin, I. Tegen, J. M. Prospero, B. Holben, O. Dubovik, and S.-J. Lin (2001),  
 1001 Sources and distributions of dust aerosols simulated with the GOCART model, J.  
 1002 Geophys. Res., 106, 22 255–22 274.

1003 Ginoux, P., L. W. Horowitz, V. Ramaswamy, I. V. Geogdzhayev, B. N. Holben, G. Stenchikov,  
 1004 and X. Tie (2006), Evaluation of aerosol distribution and optical depth in the Geophysical  
 1005 Fluid Dynamics Laboratory coupled model CM2.1 for present climate, J. Geophys. Res.,  
 1006 111, DOI: 10.1029/2005JD006707. Golaz, J.-C., M. Salzmann, L. J. Donner, L. W.  
 1007 Horowitz, Y. Ming, and M. Zhao (2011), Sensitivity of the aerosol indirect effect to  
 1008 subgrid variability in the cloud parameterization of the GFDL Atmosphere General  
 1009 Circulation Model AM3. J. Climate, 24(13), doi:10.1175/2010JCLI3945.1.

1010 Granier, C., A. Guenther, J.-F. Lamarque, A. Mieville, J. Muller, J. Olivier, J. Orlando, J. Peters,  
 1011 G. Petron, G. Tyndall, and S. Wallens (2005), POET, a database of surface emissions of  
 1012 ozone precursors, available at: <http://www.aero.jussieu.fr/projet/ACCENT/POET.php>,  
 1013 2005.

1014 Griffies, S. M., M. Winton, L. J. Donner, L. W. Horowitz, S. M. Downes, R. Farneti, A.  
 1015 Gnanadesikan, W. J. Hurlin, H. C. Lee, Z. Liang, J. B. Palter, B. L. Samuels, A. T.  
 1016 Wittenberg, B. Wyman, J. Yin, and N. Zadeh (2011), The GFDL CM3 coupled climate  
 1017 model: characteristics of the ocean and sea ice simulations, J. Clim., 24, doi:  
 1018 10.1175/2011JCLI3964.1.

1019 Hansen, J. E., M. Sato, R. Ruedy, A. Lacis, and V. Oinas (2000), Global warming in the twenty-  
1020 first century: An alternative scenario, *Proc. Natl. Acad. Sci.*, 97, 9875-9880.

1021 Hansen, J., et al. (2005), Efficacy of climate forcings, *J. Geophys. Res.*, 110, D18104,  
1022 doi:10.1029/2005JD005776.

1023 Hanson, D. R., and K. Mauersberger (1988), Laboratory studies of nitric acid trihydrate:  
1024 implications for the south polar stratosphere, *Geophys. Res. Lett.*, 15, 855-858.

1025 Haywood, J., L. Donner, A. Jones, J.-C. Golaz (2009), Global indirect radiative forcing caused  
1026 by aerosols: IPCC (2007) and beyond in *Clouds in the Perturbed Climate System: Their*  
1027 *relationship to energy balance, atmospheric dynamics, and precipitation* by J.  
1028 Heintzenberg and R. J. Charlson, pp. 451-567, MIT press.

1029 Henderson, S. C., U. K. Wickrama, et al. (1999), Aircraft emissions: current inventories and  
1030 future scenarios in *Aviation and the Global Atmosphere*, edited by J. Penner et al., chap 9,  
1031 pp 291-331, Cambridge University Press, New York.

1032 Hendricks, J., B. Kärcher, A. Döpelheuer, J. Feichter, U. Lohmann, and D. Baumgardner (2004),  
1033 Simulating the global atmospheric black carbon cycle: a revisit to the contribution of  
1034 aircraft emissions, *Atmos. Chem. Phys.*, 4, 3521-2541.

1035 Henne, S., D. Brunner, D. Folini, S. Solberg, J. Klausen, and D. Buchmann (2010), Assessment  
1036 of parameters describing representativeness of air quality in-situ measurement sites,  
1037 *Atmos. Chem. Phys.*, 10, 3561-3581. Herman, R., S. Kulawik, et al. (2011), *Earth*  
1038 *Observing System (EOS) Tropospheric Emission Spectrometer (TES) Data Validation*  
1039 *Report (Version F06\_08), Version 5.0, JPL Internal Report D-33192, April 8, 2012*

1040 (available at  
 1041 [http://eosweb.larc.nasa.gov/PRODOCS/tes/UsersGuide/TES\\_L2\\_Data\\_Users\\_Guide.pdf](http://eosweb.larc.nasa.gov/PRODOCS/tes/UsersGuide/TES_L2_Data_Users_Guide.pdf))  
 1042 Hess, P. G., S. Flocke, J.-F. Lamarque, M. C. Barth, and S. Madronich (2000), Episodic,  
 1043 modeling of the chemical structure of the troposphere as revealed during the spring  
 1044 MLOPEX 2 intensive, J. Geophys. Res., 105, doi:10.1029/2000JD900253.  
 1045 Holloway, T., H. Levy II, and P. Kasibhatla (2000), Global distribution of carbon monoxide, J.  
 1046 Geophys. Res., 105, D10, 12123-12147.  
 1047 Ho, S., D. P. Edwards, J. C. Gille, M. Luo, G. B. Osterman, S. S. Kulawik, and H. Worden  
 1048 (2009), A global comparison of carbon monoxide profiles and column amounts from  
 1049 Tropospheric Emission Spectrometer (TES) and Measurements of Pollution in the  
 1050 Troposphere (MOPITT), J. Geophys. Res., 114, D21307, doi:10.1029/2009JD012242.  
 1051 Horowitz, L. W., S. Walters, D. L. Mauzerall, L. K. Emmons, P. J. Rasch, C. Granier, X. Tie, J.-  
 1052 F. Lamarque, M. G. Schultz, G. S. Tyndall, J. J. Orlando, and G. P. Brasseur (2003), A  
 1053 global simulation of tropospheric ozone and related tracers: description and evaluation of  
 1054 MOZART, version 2, J. Geophys. Res., 108, D24, 4784, doi:10.1029/2002JD002853.  
 1055 Horowitz, L. W. (2006), Past, present, and future concentrations of tropospheric ozone and  
 1056 aerosols: methodology, ozone evaluation and sensitivity to aerosol wet removal, J.  
 1057 Geophys. Res., 111, D22211, doi:10.1029/2005JD006937.  
 1058 Horowitz, L. W., A. M. Fiore, G. P. Milly, R. C. Cohen, A. Perring, P. J. Wooldridge, P. G.  
 1059 Hess, L. K. Emmons, and J.-F. Lamarque (2007), Observational constraints on the

1060 chemistry of isoprene nitrates over the eastern United States, *J. Geophys. Res.*, 112  
 1061 D12S08, doi:10.1029/2006JD007747.

1062 Isaksen, I. S. A., et al. (2009), Atmospheric composition change: chemistry-climate interactions,  
 1063 *Atmos. Environ.*, 43, 5138-5192, doi:10.1016/j.atmos.env.2009.08.003.

1064 Jackson, S. C. (2009), Parallel pursuit of near-term and long-term climate mitigation, *Science*,  
 1065 326, 526-527.

1066 Jaffe, D., A. Mahura, J. Kelley, J. Atkins, P. C. Novelli, and J. Merrill (1997), Impact of Asian  
 1067 emissions on the remote North Pacific atmosphere: interpretation of CO data from  
 1068 Shemya, Guam, Midway, and Mauna Loa, *J. Geophys. Res.*, 102, 28,627-28,635.

1069 John, J., A. M. Fiore, V. Naik, and L. W. Horowitz, and J. P. Dunne (2012), Climate versus  
 1070 emission drivers of methane lifetime from 1860-2100, *Atmos. Chem. Phys.*, 12, 12021-  
 1071 12036, doi:10.5194/acp-12-12021-2012.

1072 Jöckel, P., H. Tost, A. Pozzer, C. Brühl, J. Buchholz, L. Ganzeveld, P. Hoor, A. Kerkweg, M. G.  
 1073 Lawrence, R. Sander, B. Steil, G. Stiller, M. Tanarhte, D. Taraborrelli, J. van Aardenne,  
 1074 and J. Lelieveld (2006), The atmospheric chemistry general circulation model  
 1075 ECAM5/MESSy1: consistent simulation of ozone from the surface to the mesosphere,  
 1076 *Atmos. Chem. Phys.*, 6, 5067-5104.

1077 Kanakidou, et al. (2005), Organic aerosol and global climate modeling: a review, *Atmos. Chem.*  
 1078 *Phys.*, 5, 1053-1123, 1680-7324/acp/2005-5-1053.

1079 Koch, D., S. E. Bauer, A. Del Genio, G. Faluvegi, J. R. McConnell, S. Menon, R. L. Miller, D.  
 1080 Rind, R. Ruedy, G. A. Schmidt, and D. Shindell (2011): Coupled aerosol-chemistry–

1081 climate twentieth-century transient model investigation: trends in short-lived species and  
 1082 climate responses, *J. Climate*, 24, 2693–2714.

1083 Koch, D., and A. D. Del Genio (2010), Black carbon semi-direct effects on cloud cover: review  
 1084 and synthesis, *Atmos. Chem. Phys.*, 10, 7685-7696, doi:10.5194/acp-10-7685-2010.

1085 Koch, D., S. Menon, A. Del Genio, R. Ruedy, I. Aleinov, and G. A. Schmidt (2009),  
 1086 Distinguishing aerosol impacts on climate over the past century, *J. Climate*, 22, 2659-  
 1087 2677.

1088 Krol, M., P. J. van Leeuwen, and J. Lelieveld (1998), Global OH trend inferred from methyl  
 1089 chloroform measurements, *J. Geophys. Res.*, 103, D9, 10697-10711.

1090 Krol, M., and J. Lelieveld (2003), Can the variability in tropospheric OH be deduced from  
 1091 measurements of 1,1,1-trichloroethane (methyl chloroform)? *J. Geophys. Res.*, 108(D3),  
 1092 doi:10.1029/2002JD002423.

1093 Kulawik, S. S., J. Worden, A. Eldering, K. Bowman, M. Gunson, G. B. Osterman, L. Zhang, S.  
 1094 Clough, M. W. Shephard, and R. Beer (2006), Implementation of cloud retrievals for  
 1095 Tropospheric Emission Spectrometer (TES) atmospheric retrievals: part 1. Description  
 1096 and characterization of errors on trace gas retrievals, *J. Geophys. Res.*, 111, D24204,  
 1097 doi:10.1029/2005JD006733.

1098 Lamarque, J.-F., J. T. Kiehl, P. G. Hess, W. D. Collins, L. K. Emmons, P. Ginoux, C. Luo, and  
 1099 X. X. Tie (2005a), Response of a coupled chemistry-climate model to changes in aerosol  
 1100 emissions: Global impact on the hydrological cycle and the tropospheric burden of OH,  
 1101 ozone, and NO<sub>x</sub>, *Geophys. Res. Lett.*, 32, L16809, doi:10.1029/2005GL023419.

1102 Lamarque, J.-F., P. Hess, L. Emmons, L. Buja, W. Washington, and C. Granier (2005b),  
 1103 Tropospheric ozone evolution between 1890 and 1990, *J. Geophys. Res.*, 110, D08304,  
 1104 doi:10.1029/2004JD005537.

1105 Lamarque, J.-F., et al. (2010), Historical (1850–2000) gridded anthropogenic and biomass  
 1106 burning emissions of reactive gases and aerosols: methodology and application, *Atmos.*  
 1107 *Chem. Phys.*, 10, doi:10.5194/acp-10-7017-2010, 7017-7039.

1108 Lamarque, J.-F., G. P. Kyle, M. Meinshausen, K. Riahi, S. H. Smith, D. P. van Vuuren, A. J.  
 1109 Conley, and F. Vitt (2011), Global and regional evolution of short-lived radiatively-active  
 1110 gases and aerosols in the Representative Concentration Pathways, *Climatic Change*, 109,  
 1111 10.1007/s10584-011-0155-0, 191-212.

1112 Lamarque, J.-F., L. K. Emmons, P. G. Hess, D. E. Kinnison, S. Tilmes, F. Vitt, C. L. Heald, E.  
 1113 A. Holland, P. H. Lauritzen, J. Neu, J. J. Orlando, P. J. Rasch, and G. K. Tyndall (2012),  
 1114 CAM-chem: description and evaluation of interactive atmospheric chemistry in the  
 1115 Community Earth System Model, *Geosci. Model. Dev.*, 5, 369-411, doi:10.5194/gmd-5-  
 1116 369-2012.

1117 Lawrence, M. G., P. Jöckel, and R. von Kuhlmann (2001), What does the global mean OH  
 1118 concentration tell us?, *Atmos. Phys. Chem.*, 1, 37-49.

1119 Lee, D. S., B. Owen, A. Graham, C. Fichter, L. L. Lin, and D. Dimitriu (2005), Allocation of  
 1120 International Aviation emissions from scheduled air traffic – present day and historical  
 1121 (Report 2 of 3), Manchester Metropolitan University, Center for Air Transport and the  
 1122 Environment, CATE-2005-3(C)-2, Manchester, UK.

1123 ([http://www.cate.mmu.ac.uk/documents/projects/mmuallocationsreport2currentdayv1\\_5.](http://www.cate.mmu.ac.uk/documents/projects/mmuallocationsreport2currentdayv1_5.pdf)  
 1124 [pdf](http://www.cate.mmu.ac.uk/documents/projects/mmuallocationsreport2currentdayv1_5.pdf)).

1125 Lelieveld, J., W. Peters, F. J. Dentener, and M. C. Krol (2002), Stability of tropospheric hydroxyl  
 1126 chemistry, J. Geophys. Res., 107, D23, doi:10.1029/2002JD002272.

1127 Levy II, H. (1971), Normal atmosphere: Large radical and formaldehyde concentrations  
 1128 predicted, Science, 173, 141-143.

1129 Levy II, H., M Daniel Schwarzkopf, L. W Horowitz, V. Ramaswamy, and K. L. Findell (2008),  
 1130 Strong sensitivity of late 21st Century climate to projected changes in short-lived air  
 1131 pollutants, J. Geophys. Res., 113, D06102, DOI:10.1029/2007JD009176.

1132 Levy II, H., L. W. Horowitz, M. D. Schwarzkopf, Y. Ming, J.-C. Golaz, V. Naik, and V.  
 1133 Ramaswamy (2013), The roles of aerosol direct and indirect effects in past and future  
 1134 climate change, J. Geophys. Res, in press.

1135 Li, F., P. Ginoux, and V. Ramaswamy (2008), Distribution, transport, and deposition of mineral  
 1136 dust in the Southern Ocean and Antarctica: contribution of major sources, J. Geophys.  
 1137 Res., 113, D10207, doi:10.1029/2007JD009190.

1138 Liao, H., P. J. Adams, S. H. Chung, J. H. Seinfeld, L. J. Mickley, and D. J. Jacob (2003),  
 1139 Interactions between tropospheric chemistry and aerosols in a unified general circulation  
 1140 model, J. Geophys. Res., 108(D1), 4001. Liao, H. and J. H. Seinfeld (2005), Global  
 1141 impacts of gas-phase chemistry-aerosol interactions on direct radiative forcing by  
 1142 anthropogenic aerosols and ozone, J. Geophys. Res., 110, D18208,  
 1143 doi:10.1029/2005JD005907.

1144 Liao, H., Y. Zhang, W.-T. Chen, F. Raes, and J. H. Seinfeld (2009), Effect of chemistry-aerosol-  
 1145 coupling on predictions of future climate and future levels of tropospheric ozone and  
 1146 aerosols, *J. Geophys. Res.*, 114, D10306, doi:10.1029/2008JD010984.

1147 Lin, M., et al. (2012), Transport of Asian ozone pollution into surface air over the western  
 1148 United States in spring, *J. Geophys. Res.*, 117, D00V07, doi:10.1029/2011JD016961.

1149 Liu, H., D.J. Jacob, I. Bey, and R.M. Yantosca (2001), Constraints from  $^{210}\text{Pb}$  and  $^7\text{Be}$  on wet  
 1150 deposition and transport in a global three-dimensional chemical tracer model driven by  
 1151 assimilated meteorological fields, *J. Geophys. Res.*, 106(D11), 12,109-12,128.

1152 Logan, J. A., M. J. Prather, S. C. Wofsy, and M. B. McElroy (1981), Tropospheric chemistry: a  
 1153 global perspective, *J. Geophys. Res.*, 86, C8, 7210-7254.

1154 Logan, J. A. (1999), An analysis of ozonesonde data for the troposphere: Recommendations for  
 1155 testing 3-D models, and development of a gridded climatology for tropospheric ozone, *J.*  
 1156 *Geophys. Res.*, 104, 16,115-16,149.

1157 Lohmann, U., and J. Feichter (2005), Global indirect aerosol effects: a review, *Atmos. Chem.*  
 1158 *Phys.*, 5, 715-737.

1159 Lohmann, U., L. Rotstayn, T. Storelvmo, A. Jones, S. Menon, J. Quaas, A. M. L. Ekman, D.  
 1160 Koch, and R. Ruedy (2010), Total aerosol effect: radiative forcing or radiative flux  
 1161 perturbation?, *Atmos. Chem. Phys.*, 10, 3235-3246.

1162 Lopez, J. P., M. Luo, L. E. Christensen, M. Loewenstein, H. Jost, C. R. Webster, and G.  
 1163 Osterman (2008), TES carbon monoxide validation during two AVE campaigns using the

1164 Argus and ALIAS instruments on NASA's WB-57F, *J. Geophys. Res.*, 113, D16S47,  
 1165 doi:10.1029/2007JD008811.

1166 Luo, M., et al. (2007a), Comparison of carbon monoxide measurements by TES and MOPITT:  
 1167 Influence of in situ data and instrument characteristics on nadir atmospheric species  
 1168 retrievals, *J. Geophys. Res.*, 112, D09303, doi:10.1029/2006JD007663.

1169 Luo, M., et al. (2007b), TES carbon monoxide validation with DACOM aircraft measurements  
 1170 during INTEx-B 2006, *J. Geophys. Res.*, 112, D24S48, doi:10.1029/2007JD008803.

1171 Madronich, S., and S. Flocke (1998), The role of solar radiation in atmospheric chemistry,  
 1172 Handbook of Environmental Chemistry, P. Boule, ed., Springer-Verland, Heidelberg, pp  
 1173 1-26.

1174 Mahowald, N., D. S. Ward, S. Kloster, M. G. Flanner, C. L. Heald, N. G. Heavens, P. G. Hess,  
 1175 J.-F. Lamarque, and P. Y. Chuang (2011), Aerosol impacts on climate and  
 1176 biogeochemistry, *Ann. Rev. Environ. Res.*, 36, 10.1146/annurev-environ-042009-094507.

1177 Mao, J., et al. (2009) Airborne measurement of OH reactivity during INTEx-B, *Atmos. Chem.*  
 1178 *Phys.*, 9, 163-173, doi:10.5194/acp-9-163-2009.

1179 Mao, J., S. Fan, D. J. Jacob, and K. R. Travis (2013), Radical loss in the atmosphere from Cu-Fe  
 1180 redox coupling in aerosols, *Atmos. Chem. Phys.*, 13, 509-519, doi:10.5194/acp-13-509-  
 1181 2013.

1182 Martin, R.V., D. J. Jacob, R. M. Yantosca, M. Chin, and P. Ginoux (2003), Global and regional  
 1183 decreases in tropospheric oxidants from photochemical effects of aerosols, *J. Geophys.*  
 1184 *Res.*, 108(D3), 4097, doi:10.1029/2002JD002622.

1185 Meinshausen, M., S. J. Smith, K. V. Calvin, J. S. Daniel, M. Kainuma, J.-F. Lamarque, K.  
 1186 Matsumoto, S. A. Montzka, S. C. B. Raper, K. Riahi, A. M. Thomson, G. J. M. Velders  
 1187 and D. van Vuuren (2011), The RCP Greenhouse Gas Concentrations and their Extension  
 1188 from 1765 to 2300, *Climatic Change* (Special Issue), doi:10.1007/s10584-011-0156-z.

1189 Menon, S., N. Unger, D. Koch, J. Francis, T. Garrett, I. Sednev, D. Shindell, and D. Streets  
 1190 (2008), Aerosol climate effects and air quality impacts from 1980 to 2030. *Environ. Res.*  
 1191 *Lett.*, 3, 024004, doi:10.1088/1748-9326/3/2/024004.

1192 Ming, Yi, and V Ramaswamy (2009), Nonlinear climate and hydrological responses to aerosol  
 1193 effects, *J. Climate*, 22(6), 1329-1339.

1194 Molina, M., D. Zaelke, K. Madhava Sarma, S. O. Andersen, V. Ramanathan, and D. Kaniaru  
 1195 (2009), Reducing abrupt climate change risk using the Montreal Protocol and other  
 1196 regulatory actions to complement cuts in CO<sub>2</sub> emissions, *Proc. Natl. Acad. Sci.*, 106,  
 1197 20616-20621.

1198 Monahan, E. C., D. E. Spiel, and K. L. Davidson (1986), A model of marine aerosol generation  
 1199 via whitecaps and wave disruption, *Oceanic Whitecaps*, E. C. Monahan and G.  
 1200 MacNiocaill, Eds., pp167–174, Reidel, Dordrecht, The Netherlands.

1201 Montzka, S. A., C. M. Spivakovsky, J. H. Butler, J. W. Elkins, L. T. Lock, and D. J. Mondeel  
 1202 (2000), New observational constraints, for atmospheric hydroxyl on global and  
 1203 hemispheric scales, *Science*, 288, 500-503.

1204 Montzka, S. A., M. Krol, E. Dlugokencky, B. Hall, P. Jöckel, and J. Lelieveld (2011), Small  
 1205 interannual variability of global atmospheric hydroxyl, *Science*, 331, 67-69.

1206 Naik, V., D. Mauzerall, L. Horowitz, D. Schwarzkopf, V. Ramaswamy, and M. Oppenheimer  
 1207 (2005), Net radiative forcing due to changes in regional emissions of tropospheric ozone  
 1208 precursors, *J. Geophys. Res.*, 110, doi:10.1029/2005JD005908.

1209 Naik, V. et al. (2012), Preindustrial to present day changes in tropospheric hydroxyl radical and  
 1210 methane lifetime from the Atmospheric Chemistry and Climate Model Intercomparison  
 1211 Project (ACCMIP), *Atmos. Chem. Phys. Discuss.*, 12, 30755–30804, doi:10.5194/acpd-  
 1212 12-30755-2012.

1213 Naja, M., and S. Lal (2002), Surface ozone and precursor gases at Gadanki (13.5°N, 79.2°E), a  
 1214 tropical rural site in India, *J. Geophys. Res.*, 107, D14,4197, 10.1029/2001JD000357.

1215 Naja, M., S. Lal, and D. Chand (2003), Diurnal and seasonal variabilities in surface ozone at a  
 1216 high altitude site M. Abu (24.6°N, 72.7°E, 1680 m asl) in India, *Atmos. Environ.*, 37,  
 1217 4205-4215.

1218 Nassar, R., et al. (2008), Validation of Tropospheric Emission Spectrometer (TES) Nadir Ozone  
 1219 Profiles Using Ozonesonde Measurements, *J. Geophys. Res.*, 113, D15S17,  
 1220 doi:10.1029/2007JD008819.

1221 Novelli, P. C., K. A. Masarie, and P. M. Lang (1998), Distributions and recent changes of carbon  
 1222 monoxide in the lower troposphere, *J. Geophys. Res.*, 103, 19,015-19,033.

1223 Novelli, P.C. and K.A. Masarie (2010), Atmospheric Carbon Monoxide Dry Air Mole Fractions  
 1224 from the NOAA ESRL Carbon Cycle Cooperative Global Air Sampling Network, 1988-  
 1225 2009, Version: 2010-07-14, path: <ftp://ftp.cmdl.noaa.gov/ccg/co/flask/event/>  
 1226 (downloaded on August 10, 2010).

1227 O'Dowd C. D., M.C. Facchini, F. Cavalli, D. Ceburnis, M. Mircea, S. Decesari, S. Fuzzi, Y. J.  
 1228 Yoon, and J. P. Putaud (2004), Biogenically-driven organic contribution to marine  
 1229 aerosol, *Nature*, 431, 676–780.

1230 Parrella, J. P., et al. (2012), Tropospheric bromine chemistry: implications for present and pre-  
 1231 industrial ozone and mercury, *Atmos. Chem. Phys.*, 12(15), 6723-6740.

1232 Penner, J. E., M. J. Prather, I. S. A. Isaksen, J. S. Fuglestad, Z. Klimont and D. S. Stevenson  
 1233 (2010), Short-lived uncertainty? *Nature Geosci.*, 3, 587-588.

1234 Philipona, R., K. Behrens, and C. Ruckstuhl (2009), How declining aerosols and rising  
 1235 greenhouse gases forced rapid warming in Europe since the 1980s, *Geophys. Res. Lett.*,  
 1236 36, L02806, doi:10.1029/2008GL036350.

1237 Prather, M. J., D. Ehhalt, F. Dentener, et al. (2001), Atmospheric chemistry and greenhouse  
 1238 gases , in *Climate Change 2001: The Scientific Basis. Contribution of Working Group I*  
 1239 *to the Third Assessment Report of the Intergovernmental Panel on Climate Change*,  
 1240 edited by J. T. Houghton, et al., pp 239-287, Cambridge Univ. Press, New York.

1241 Prather, M., C. Holmes, and J. Hsu (2012), Reactive greenhouse gas scenarios: systematic  
 1242 exploration of uncertainties and the role of atmospheric chemistry, *Geophys. Res. Lett.*,  
 1243 39, L09803, doi:10.1029/2012GL051440.

1244 Price, C., and D. Rind (1994), Possible implications of global climate change on global lightning  
 1245 distributions and frequencies, *J. Geophys. Res.*, 99, 10823-10831, doi:  
 1246 10.1029/94JD00019.

1247 Prinn, R. G., R. F. Weiss, B. R. Miller, J. Huang, F. N. Alyea, D. M. Cunnold, P. J. Fraser, D. E.  
 1248 Hartley, and P. G. Simmonds (1995), Atmospheric trends and lifetime of  $\text{CH}_3\text{CCl}_3$  and  
 1249 global OH concentrations, *Science*, 269, 187.

1250 Prinn, R., J. Huang, R. F. Weiss, D. M. Cunnold, P. J. Fraser, P. G. Simmonds, A. McCullough,  
 1251 C. Harth, P. Salameh, S. O'Doherty, R. H. J. Wang, L. Porter, and B. R. Miller (2001),  
 1252 Evidence for substantial variations of atmospheric hydroxyl radicals in the past two  
 1253 decades, *Science*, 292, 1882.

1254 Rasmussen, D. J., A. M. Fiore, V. Naik, L. W. Horowitz, S. J. McGinnis, and M. G. Schultz  
 1255 (2012), Surface ozone-temperature relationships in the eastern US: a monthly  
 1256 climatology for evaluating chemistry-climate models, *Atmos. Environ.*, 47, doi:  
 1257 10.1016/j.atmosenv.2011.11.021.

1258 Rayner, N. A., D. E. Parker, E. B. Horton, C. K. Folland, L. V. Alexander, and D. P. Rowell  
 1259 (2003), Global analyses of sea surface temperature, sea ice, and night marine air  
 1260 temperature since the late nineteenth century, *J. Geophys. Res.*, 108,  
 1261 doi:10.1029/2002JD002670.

1262 Reeve, N., and R. Toumi (1999), Lightning activity as an indication of climate change, *Q. J. R.*  
 1263 *Meteorol. Soc.*, 125, 893-903.

1264 Reddy, R. R., K. R. Gopal, L. S. S. Reddy, K. Narasimhulu, K. R. Kumar, Y. N. Ahammed, and  
 1265 C. V. K. Reddy (2008), Measurements of surface ozone at semi-arid site Ananatapur  
 1266 (14.62°N, 77.65°E, 331 m asl) in India, *J. Atmos. Chem.*, 59, 47-59.

1267 Reidmiller, D., A. M. Fiore, D. A. Jaffe, D. Bergmann, et al. (2009), The influence of foreign vs.  
 1268 North American emissions on surface ozone in the U.S., *Atmos. Chem. Phys.*, 9, 5027-  
 1269 5042.

1270 Rosenfeld, D., U. Lohmann, G. B. Raga, C. O'Dowd, M. Kulmala, S. Fuzzi, A. Reissell, M. O.  
 1271 Andreae (2008), Flood or drought: how do aerosols affect precipitation?, *Science*, 321,  
 1272 1309-1313.

1273 Ruckstuhl, C., et al. (2008), Aerosol and cloud effects on solar brightening and the recent rapid  
 1274 warming, *Geophys. Res. Lett.*, 35, L12708, doi:10.1029/2008GL034228. Sander, S. P., R.  
 1275 R. Friedl, D. M. Golden, M. J. Kurylo, G. K. Moortgat, H. Keller-Rudek, P. H. Wine, A.  
 1276 R. Ravishankara, C. E. Kolb, M. J. Molina, B. J. Finlayson-Pitts, R. E. Huie, and V. L.  
 1277 Orkin, Chemical kinetics and photochemical data for use in atmospheric studies,  
 1278 Evaluation No. 15, JPL Publications 06-2, 2006, Jet Propulsion Laboratory, Pasadena,  
 1279 CA, USA.

1280 Schumann, U. and H. Huntrieser (2007), The global lightning-induced nitrogen oxides source,  
 1281 *Atmos. Chem. Phys.*, 7, 3823-3907, doi:10.5194/acp-7-3823-2007.

1282 Shindell, D. T., et al. (2006a), Multimodel simulations of carbon monoxide: Comparison with  
 1283 observations and projected near-future changes, *J. Geophys. Res.*, 111, D19306,  
 1284 doi:10.029/2006JD007100.

1285 Shindell, D. T., G. Faluvegi, N. Unger, E. Aguilar, G. A. Schmidt, D. M. Koch, S. E. Bauer, and  
 1286 R. L. Miller (2006b), Simulations of preindustrial, present-day, and 2100 conditions in  
 1287 the NASA GISS composition and climate model G-PUCCINI, *Atmos. Chem. Phys.*, 6,  
 1288 4427-4459.

1289 Shindell, D. T., G. Faluvegi, S. E. Bauer, D. Koch, N. Unger, S. Menon, R. L. Miller, G. A.  
 1290 Schmidt, and D. G. Streets (2007), Climate response to projected changes in short-lived  
 1291 species under the A1B scenario from 2000-2050 in the GISS climate model. *J. Geophys.*  
 1292 *Res.*, 112, D20103, doi:10.1029/2007JD008753.

1293 Shindell, D. T., H. Levy, II, M. D. Schwarzkopf, L. W. Horowitz, J.-F. Lamarque, and G.  
 1294 Faluvegi (2008), Multimodel projections of climate change from short-lived emissions  
 1295 due to human activities. *J. Geophys. Res.*, 113, D11109, doi:10.1029/2007JD009152.

1296 Shindell, D. T. and J.-F. Lamarque (2011), The atmospheric Chemistry and Climate Model Inter-  
 1297 comparison Project (ACCMIP), *IGAC News*, 45, 9-14.

1298 Shindell, D. T., et al. (2012a), Simultaneously mitigating near-term climate change and  
 1299 improving human health and food security, *Science*, 335, 183-189,  
 1300 doi:10.1126/science.1210026.

1301 Shindell, D. T., et al. (2012b), Radiative forcing in the ACCMIP historical and future climate  
 1302 simulations, *Atmos. Chem. Phys. Discuss.*, 12, 21105-21210, doi:10.5194/acpd-12-  
 1303 21105-2012.

1304 Skeie, R. B., T. K. Berntsen, G. Myhre, K. Tanaka, M. M. Kvalevåg, and C. R. Hoyle (2011),  
 1305 Anthropogenic radiative forcing time series from pre-industrial times until 2010, *Atmos.*  
 1306 *Chem. Phys.*, 11, doi:10.5194/acp-11-11827-2011.

1307 Stevenson, D. S., F. J. Dentener, M. Schultz, et al. (2006), Multi-model ensemble simulations of  
 1308 present day and near-future tropospheric ozone, *J. Geophys. Res.*, 111, D08301,  
 1309 doi:10.1029/2005JD006338.

1310 Spivakovsky, C. M., J. A. Logan, S. A., Montzka, Y. J. Balkanski, M. Foreman-Fowler, D. B. A.  
 1311 Jones, L. W. Horowitz, A. C. Fusco, C. A. M. Brenninkmeijer, M. J. Prather, S. C.  
 1312 Wofsy, and M. B. McElroy (2000), Three-dimensional climatological distribution of  
 1313 tropospheric OH: Update and evaluation, *J. Geophys. Res.*, 105, D7, 8931-8980.

1314 Tie, X. X., S. Madronich, S. Walters, D. P. Edwards, P. Ginoux, N. Mahowald, R. Y. Zhang, C.  
 1315 Lou, and G. Brasseur (2005), Assessment of the global impact of aerosols on  
 1316 tropospheric oxidants, *J. Geophys. Res.*, 110, D03204, doi:10.1029/2004JD005359.

1317 Tilmes, S., J.-F. Lamarque, L. K. Emmons, A. Conley, M. G. Schultz, M. Saunois, V. Thouret,  
 1318 A. M. Thompson, S. J. Oltmas, B. Johnson, and D. Tarasick (2012), Ozone-sonde  
 1319 climatology between 1995 and 2009: description, evaluation, and applications, *Atmos.*  
 1320 *Chem. Phys.* 12, 7475-7497, doi:10.5194/acp-12-7475-2012.

1321 Tong, D. Q., and D. L. Mauzerall (2006), Spatial variability of summertime tropospheric ozone  
 1322 over the continental United States: Implications of an evaluation of the CMAQ model,  
 1323 *Atmos. Environ.*, 40, doi:10.1016/j.atmosenv.2005.11.058, 3041-3056.

1324 Tost, H., P. Jöckel, and J. Lelieveld (2007), Lightning and convection parameterizations –  
 1325 uncertainties in global modelling, *Atmos. Chem. Phys.*, 7, 4553-4568, doi:10.5194/acp-7-  
 1326 4553-2007.

1327 Tsigaridis, K., M. Krol, F.J. Dentener, Y. Balkanski, J. Lathière, S. Metzger, D.A. Hauglustaine,  
 1328 and M. Kanakidou (2006), Change in global aerosol composition since preindustrial  
 1329 times, *Atmos. Chem. Phys.*, 6, 5143-5162, doi:10.5194/acp-6-5143-2006.

1330 Unger, N., D. T. Shindell, D. M. Koch, and D. G. Streets (2006), Cross influences of ozone and  
 1331 sulfate precursor emissions changes on air quality and climate, *Proc. Natl. Acad. Sci.*,  
 1332 103, 4377-4380, doi:10.1073/pnas.0508769103.

1333 Unger, N., S. Menon, D.M. Koch, and D.T. Shindell (2009), Impacts of aerosol-cloud  
 1334 interactions on past and future changes in tropospheric composition, *Atmos. Chem. Phys.*,  
 1335 9, 4155-4129, doi:10.5194/acp-9-4115-2009.

1336 van der Werf, G. R., J. T. Randerson, L. Giglio, G. J. Collatz, P. S. Kasibhatla, A. F. Arellano  
 1337 (2006), Interannual variability in global biomass burning emissions from 1997 to 2004,  
 1338 *Atmos. Chem. Phys.*, 6, 3423-3441.

1339 Voulgarakis, A. et al. (2012), Analysis of present day and future OH and methane lifetime in the  
 1340 ACCMIP simulations, *Atmos. Chem. Phys. Discuss.*, 12, 22945–23005,  
 1341 doi:10.5194/acpd-12-22945-2012.

1342 Waliser, D. E., and C. Gautier (1993), A satellite derived climatology of the ITCZ, *J. Clim.*, 6,  
 1343 2162-2174.

1344 Wang, Y., J. A. Logan, and D. J. Jacob (1998), Global simulation of tropospheric O<sub>3</sub>-NO<sub>x</sub>-  
 1345 hydrocarbon chemistry, 2. Model evaluation and global ozone budget, *J. Geophys. Res.*,  
 1346 103(D9), 10,727-10,756.

1347 Wayne, R. P. (1991), *Chemistry of Atmospheres: An introduction to the chemistry of*  
 1348 *atmospheres of Earth, the planets and their satellites*, 2<sup>nd</sup> edition, Oxford University Press,  
 1349 New York.

1350 Wesely, M. L. (1989), Parameterization of surface resistance to gaseous dry deposition in  
 1351 regional-scale numerical models, *Atmos. Environ.*, 23, 1293-1304.

1352 West, J. J., A. M. Fiore, V. Naik, L. W. Horowitz, M. D. Schwarzkopf, and D. L. Mauzerall  
 1353 (2007), Ozone air quality and radiative forcing consequences of changes in ozone  
 1354 precursor emissions, *Geophys. Res. Lett.*, 34, L06806, 10.1029/2006GL029173.

1355 Williams, E. R. (2009), The global electrical circuit: a review, *Atmos. Res.*, 91, 140-152,  
 1356 doi:10.1016/j.atmosres.2008.05.018. Wild, O. (2007), Modeling the global tropospheric  
 1357 ozone budget: exploring the variability in current models, *Atmos. Chem. Phys.*, 7,  
 1358 doi:10.5194/acp-7-2643-2007, 2643-2660.

1359 Wild, O., M. J. Prather, and H. Akimoto (2001), Indirect long-term global radiative cooling from  
 1360 NO<sub>x</sub> emissions, *Geophys. Res. Lett.*, 28, 1719-1722.

1361 Wu, S., L. J. Mickley, D. J. Jacob, J. A. Logan, R. M. Yantosca, and D. Rind (2007), Why are  
 1362 there large differences between models in global budgets of tropospheric ozone?, *J.*  
 1363 *Geophys. Res.*, 112, D05302, doi:10.1029/2006JD007801.

1364 Wu, Z., et al. (2012), Evaluation and improvements of two community models in simulating dry  
 1365 deposition velocities for peroxyacetyl nitrate (PAN) over a coniferous forest, *J. Geophys.*  
 1366 *Res.*, 117(D4), D04310.

1367 Yienger, J. J., and H. Levy II (1995), Empirical model of global soil-biogenic NO<sub>x</sub> emissions, *J.*  
 1368 *Geophys. Res.*, 100(D6), 11,447–11,464, doi:10.1029/95JD00370.

1369 Young, P. J., et al. (2012), Pre-industrial to end 21st century projections of tropospheric ozone  
 1370 from the Atmospheric Chemistry and Climate Model Intercomparison Project

1371 (ACCMIP), *Atmos. Chem. Phys. Discuss*, 12, 21615–21677, doi: 10.5194/acpd-12-  
1372 21615-2012.

1373 Yuan, T., L. A. Remer, H. Bian, J. R. Ziemke, R. Albrecht, K. E. Pickering, L. Oreopoulos, S. J.  
1374 Goodman, H. Yu, and D. J. Allen (2012), Aerosol indirect effect on tropospheric ozone via  
1375 lightning, *J. Geophys. Res.*, 117, D18213, doi:10.1029/2012JD017723.

1376 **Tables**

1377 Table 1. Chemical species included in AM3. Soluble gaseous species that undergo wet  
 1378 deposition in AM3 are marked with an asterisk (\*).

No.	Species Name	Chemical Formula	Details
<b>Transported</b>			
1	O3	O <sub>3</sub>	ozone
2	N2O	N <sub>2</sub> O	nitrous oxide
3	NO	NO	nitric oxide
4	NO2	NO <sub>2</sub>	nitrogen dioxide
5	NO3	NO <sub>3</sub>	nitrate radical
6	HNO3*	HNO <sub>3</sub>	nitric acid
7	HO2NO2*	HNO <sub>4</sub>	pernitric acid
8	N2O5	N <sub>2</sub> O <sub>5</sub>	dinitrogen pentaoxide
9	CH4	CH <sub>4</sub>	methane
10	CH3OOH	CH <sub>3</sub> OOH	methyl hydroperoxide
11	CH2O*	HCHO	formaldehyde
12	CO	CO	carbon monoxide
13	H2O2*	H <sub>2</sub> O <sub>2</sub>	hydrogen peroxide
14	C3H6	C <sub>3</sub> H <sub>6</sub>	propene
15	ISOP	C <sub>5</sub> H <sub>8</sub>	isoprene
16	CH3CHO*	CH <sub>3</sub> CHO	acetaldehyde
17	POOH*	C <sub>3</sub> H <sub>6</sub> OHOH	
18	CH3COOOH*	CH <sub>3</sub> COOOH	peracetic acid
19	PAN	CH <sub>3</sub> CO <sub>3</sub> NO <sub>2</sub>	peroxy acetyl nitrate
20	ONIT*	CH <sub>3</sub> COCHO <sub>2</sub> CH <sub>2</sub> OHNO	
21	C2H6	C <sub>2</sub> H <sub>6</sub>	ethane
22	C2H4	C <sub>2</sub> H <sub>4</sub>	ethene
23	C4H10	C <sub>4</sub> H <sub>10</sub>	lumped alkanes as C ≥ 4
24	MPAN	CH <sub>2</sub> CCH <sub>3</sub> CO <sub>3</sub> NO <sub>2</sub>	methacryloyl peroxy nitrate
25	MVK*	CH <sub>2</sub> CHCOCH <sub>3</sub>	methyl vinyl ketone
26	MACR*	CH <sub>2</sub> CCH <sub>3</sub> CHO	methacrolein
27	MACROOH*	CH <sub>3</sub> COCH(OOH)CH <sub>2</sub> OH	
28	C2H5OOH*	C <sub>2</sub> H <sub>5</sub> OOH	ethyl hydroperoxide
29	C10H16	C <sub>10</sub> H <sub>16</sub>	lumped monoterpenes as α-pinene
30	C3H8	C <sub>3</sub> H <sub>8</sub>	propane
31	C3H7OOH*	C <sub>3</sub> H <sub>7</sub> OOH	propyl hydroperoxide
32	CH3COCH3	CH <sub>3</sub> COCH <sub>3</sub>	acetone
33	ROOH*	CH <sub>3</sub> COCH <sub>2</sub> OOH	
34	CH3OH*	CH <sub>3</sub> OH	methanol
35	C2H5OH*	C <sub>2</sub> H <sub>5</sub> OH	ethanol
36	GLYALD*	HOCH <sub>2</sub> CHO	glycolaldehyde
37	HYAC*	CH <sub>3</sub> COCH <sub>2</sub> OH	hydroxyacetone

38	HYDRALD <sup>*</sup>	HOCH <sub>2</sub> CCH <sub>3</sub> CHCHO	lumped unsaturated hydroxycarbonyl
39	CH <sub>3</sub> COCHO <sup>*</sup>	CH <sub>3</sub> COCHO	methyl glyoxal
40	ONITR <sup>*</sup>	CH <sub>2</sub> CCH <sub>3</sub> CHONO <sub>2</sub> CH <sub>2</sub> OH	lumped isoprene nitrate
41	XOOH <sup>*</sup>	HOCH <sub>2</sub> C(OOH)CH <sub>3</sub> CH(OH)CHO	
42	ISOPOOH <sup>*</sup>	HOCH <sub>2</sub> C(OOH)CH <sub>3</sub> CHCH <sub>2</sub>	unsaturated hydroxyhydroperoxide
43	H <sub>2</sub>	H <sub>2</sub>	molecular hydrogen
44	SO <sub>2</sub> <sup>*</sup>	SO <sub>2</sub>	sulfur dioxide
45	SO <sub>4</sub>	SO <sub>4</sub> <sup>2-</sup>	sulfate
46	DMS <sup>*</sup>	CH <sub>3</sub> SCH <sub>3</sub>	dimethyl sulfide
47	NH <sub>3</sub> <sup>*</sup>	NH <sub>3</sub>	ammonia
48	NH <sub>4</sub> NO <sub>3</sub>	NH <sub>4</sub> NO <sub>3</sub>	ammonium nitrate
49	NH <sub>4</sub>	NH <sub>4</sub> <sup>+</sup>	ammonium
50	SOA		secondary organic aerosol
51	dust1	dust	dust dry radius 0.1 – 1.0 μm
52	dust2	dust	dust dry radius 1.0 – 1.8 μm
53	dust3	dust	dust dry radius 1.8 – 3.0 μm
54	dust4	dust	dust dry radius 3.0 – 6.0 μm
55	dust5	dust	dust dry radius 6.0 – 10.0 μm
56	ssalt1	sea salt	sea salt dry radius 0.1 – 1.0 μm
57	ssalt2	sea salt	sea salt dry radius 1.0 – 1.8 μm
58	ssalt3	sea salt	sea salt dry radius 1.8 – 3.0 μm
59	ssalt4	sea salt	sea salt dry radius 3.0 – 6.0 μm
60	ssalt5	sea salt	sea salt dry radius 6.0 – 10.0 μm
61	bcphob	black carbon	hydrophobic fraction of black carbon
62	bcphil	black carbon	hydrophilic fraction of black carbon
63	omphob	organic matter	hydrophobic fraction of organic matter
64	omphil	organic matter	hydrophilic fraction of organic matter
65	HCl <sup>*</sup>	HCl	hydrochloric acid
66	HOCl	HOCl	hypochlorous acid
67	ClONO <sub>2</sub>	ClONO <sub>2</sub>	chlorine nitrate
68	Cl	Cl	elemental chlorine
69	ClO	ClO	chlorine monoxide
70	Cl <sub>2</sub> O <sub>2</sub>	Cl <sub>2</sub> O <sub>2</sub>	chlorine monoxide dimer
71	Cl <sub>2</sub>	Cl <sub>2</sub>	molecular chlorine
72	HOBr	HOBr	hypobromous acid
73	HBr <sup>*</sup>	HBr	hydrobromic acid
74	BrONO <sub>2</sub>	BrONO <sub>2</sub>	bromine nitrate
75	Br	Br	elemental bromine
76	BrO	BrO	bromine monoxide
77	BrCl	BrCl	bromine monochloride
78	H <sub>2</sub> O	H <sub>2</sub> O	water

Not transported			
79	O	O( <sup>3</sup> P)	ground state atomic oxygen
80	O1D	O( <sup>1</sup> D)	excited state atomic oxygen
81	OH	OH	hydroxyl radical
82	HO2	HO <sub>2</sub>	hydroperoxyl radical
83	CH3O2	CH <sub>3</sub> O <sub>2</sub>	methyl peroxy radical
84	ISOPO2	HOCH <sub>2</sub> C(OO)CH <sub>3</sub> CHCH <sub>2</sub>	peroxy radical derived from OH+ISOP
85	CH3CO3	CH <sub>3</sub> CO <sub>3</sub>	acetylperoxy radical
86	MACRO2	CH <sub>3</sub> COCH(OO)CH <sub>2</sub> OH	peroxy radical from OH addition to MVK, MACR
87	EO2	HOCH <sub>2</sub> CH <sub>2</sub> O <sub>2</sub>	
88	EO	HOCH <sub>2</sub> CH <sub>2</sub> O	
89	MCO3	CH <sub>2</sub> CCH <sub>3</sub> CO <sub>3</sub>	peroxy radical from reaction of OH with MACR
90	RO2	CH <sub>3</sub> COCH <sub>2</sub> O <sub>2</sub>	1-methyl vinoxy radical
91	C2H5O2	C <sub>2</sub> H <sub>5</sub> O <sub>2</sub>	ethyl peroxy radical
92	ISOPNO3	CH <sub>2</sub> CHCCH <sub>3</sub> OOCH <sub>2</sub> ONO <sub>2</sub>	peroxy isoprene nitrate
93	XO2	HOCH <sub>2</sub> C(OO)CH <sub>3</sub> CH(OH)CHO	Peroxy radical from OH+HYDRALD
94	PO2	C <sub>3</sub> H <sub>6</sub> OHO <sub>2</sub>	
95	C3H7O2	C <sub>3</sub> H <sub>7</sub> O <sub>2</sub>	propyl peroxy radical
96	H	H	hydrogen
97	N	N	elemental nitrogen

1379

Table 2. Emissions of short-lived species in AM3 for year 2000. Emissions for year 1860 are shown in parentheses.

Species	Anthropogenic	Biomass Burning	Biogenic/Soil	Oceans	Ship	Total
NO <sub>x</sub> (Tg N yr <sup>-1</sup> )	26.5 (0.7)	5.5 (4.8)	3.6 (3.6)	0.0 (0.0)	5.4 (0.1)	41.0 (9.3)
CO (Tg yr <sup>-1</sup> )	608.3 (67.3)	459.1 (322.6)	159.3 (159.3)	19.8 (19.8)	1.2 (0.03)	1247.7 (569.0)
C <sub>2</sub> H <sub>4</sub> (Tg C yr <sup>-1</sup> )	6.4 (1.1)	5.4 (3.6)	4.3 (4.3)	1.2 (1.2)	0.2 (0.01)	17.5 (10.2)
C <sub>2</sub> H <sub>6</sub> (Tg C yr <sup>-1</sup> )	2.6 (0.5)	2.5 (1.5)	0.8 (0.8)	0.8 (0.8)	0.12 (0.0)	6.8 (3.5)
C <sub>3</sub> H <sub>6</sub> (Tg C yr <sup>-1</sup> )	7.7 (1.0)	4.7 (2.8)	0.9 (0.9)	1.3 (1.3)	0.3 (0.01)	14.9 (6.0)
C <sub>3</sub> H <sub>8</sub> (Tg C yr <sup>-1</sup> )	2.8 (0.2)	1.6 (0.5)	1.6 (1.6)	1.0 (1.0)	0.4 (0.01)	7.4 (3.4)
CH <sub>2</sub> O (Tg C yr <sup>-1</sup> )	3.2 (0.1)	5.8 (4.0)	0.0 (0.0)	0.0 (0.0)	0.0 (0.0)	9.0 (4.1)
Acetone (Tg C yr <sup>-1</sup> )	2.2 (0.0)	2.9 (2.4)	24.3 (24.3)	0.0 (0.0)	0.0 (0.0)	29.4 (26.8)
CH <sub>3</sub> OH (Tg C yr <sup>-1</sup> )	0.8 (0.1)	11.9 (7.6)	228.2 (228.2)	0.0 (0.0)	0.0 (0.0)	240.9 (236.0)
C <sub>2</sub> H <sub>5</sub> OH (Tg C yr <sup>-1</sup> )	4.5 (0.6)	0.1 (0.05)	9.2 (9.2)	0.0 (0.0)	0.0 (0.0)	13.8 (9.9)
C <sub>4</sub> H <sub>10</sub> (Tg C yr <sup>-1</sup> )	43.0 (0.6)	0.9 (0.7)	0.0 (0.0)	0.0 (0.0)	1.2 (0.03)	45.1 (1.3)
Isoprene (Tg C yr <sup>-1</sup> )	0.0 (0.0)	0.8 (0.3)	564.7 (564.7)	0.0 (0.0)	0.0 (0.0)	565.5 (565.1)
Terpenes (Tg C yr <sup>-1</sup> )	0.0 (0.0)	0.4 (0.2)	143.2 (143.2)	0.0 (0.0)	0.0 (0.0)	143.6 (153.5)
H <sub>2</sub> (Tg yr <sup>-1</sup> )	21.3 (2.2)	9.6 (5.2)	3.0 (3.0)	3.0 (3.0)	0.0 (0.0)	36.9 (13.4)
NH <sub>3</sub> (Tg yr <sup>-1</sup> ) <sup>a</sup>	37.5 (7.3)	10.5 (6.1)	3.1 (3.1)	9.9 (9.9)	0.0 (0.0)	61.0 (26.5)
SO <sub>2</sub> (Tg S yr <sup>-1</sup> )	46.4 (1.5)	1.9 (1.2)	0.0 (0.0)	0.0 (0.0)	5.5 (0.1)	53.8 (2.8)
BC (Tg C yr <sup>-1</sup> )	5.0 (1.3)	2.6 (2.0)	0.0 (0.0)	0.0 (0.0)	0.1 (0.0)	7.7 (3.3)
OM (Tg C yr <sup>-1</sup> )	29.7 <sup>b</sup> (18.0) <sup>b</sup>	37.2 (28.8)	30.4 (30.4)	15.5 (15.4)	0.2 (0.0)	113.0 (92.6)
Aircraft NO (Tg N yr <sup>-1</sup> )						0.8 (0.0)
Aircraft SO <sub>2</sub> (Tg yr <sup>-1</sup> )						0.1 (0.0)
Fuel use (Tg yr <sup>-1</sup> )						122.0 (0.0)
Dust (Tg yr <sup>-1</sup> )						1221 (1237)
Sea Salt (Tg yr <sup>-1</sup> )						6188 (6324)
Dimethyl sulfide (Tg yr <sup>-1</sup> )						36.2 (36.0)

<sup>a</sup> Emissions of NH<sub>3</sub> also include 0.1 Tg yr<sup>-1</sup> from animals.

<sup>b</sup> Includes 9.6 Tg C yr<sup>-1</sup> as secondary organic aerosol from the oxidation of anthropogenic NMVOC calculated using offline butane emissions and OH concentrations.

Table 3. Summary of AM3 simulations.

	Base (1981-2007)	2000	1860
CO <sub>2</sub>	Time-varying	2000	2000
CH <sub>4</sub>	Time-varying	2000	1860*
N <sub>2</sub> O	Time-varying	2000	2000
ODSs	Time varying	2000	2000
Sea Surface Temperature (SST)/Sea Ice Cover (SIC)	Observed	1996-2005	1996-2005
Short-lived Pollutant Emissions	Time-varying	2000	1860

\* For radiation calculations, CH<sub>4</sub> was set to 2000 level.

Table 4. Annual mean global budget and burdens simulated by AM3. Average values and interannual standard deviations over the baseline 1981-2000 time period are shown in column 2. Effect of changing short-lived pollutant emissions from 1860 to 2000 levels on global budget and burdens are shown in column 3 as absolute differences (2000-1860) and percent differences in parentheses.

	Annual average (1981-2000) $\pm$ Standard Deviation	2000 – 1860
<b>Tropospheric Ozone Budget</b>		
Photochemical Production ( $\text{Tg yr}^{-1}$ )	$5753 \pm 244$	2391 (69%)
Photochemical Loss ( $\text{Tg yr}^{-1}$ )	$5092 \pm 203$	1948 (63%)
Net Photochemistry ( $\text{Tg yr}^{-1}$ )	$661 \pm 46$	444 (118%)
Dry Deposition ( $\text{Tg yr}^{-1}$ )	$1205 \pm 20$	505 (69%)
Cross-tropopause flux ( $\text{Tg yr}^{-1}$ )	$443 \pm 27$	48 (14%)
Ozone Burden ( $\text{Tg}$ )	$360 \pm 7$	103 (39%)
Global Total Column Ozone (DU)	$303 \pm 5$	16.9 (6%)
Tropospheric OH Concentration ( $\text{molec cm}^{-3}$ )	$1.05 \pm 0.02 \times 10^6$	$-0.07 \times 10^6$ (-6.8%)
Tropospheric Methane Lifetime (yr)	$8.5 \pm 0.2$	0.31 (3.6%)
Lightning $\text{NO}_x$ Emissions ( $\text{Tg N yr}^{-1}$ )	$4.5 \pm 0.2$	-0.3 (-6.4%)
Tropospheric Aerosol Optical Depth at 550 nm	0.16	0.05 (50.4%)
<b>Global Total Burdens</b>		
Carbon Monoxide ( $\text{Tg}$ )	$335 \pm 11$	158.4 (82%)
Tropospheric $\text{NO}_x$ ( $\text{Gg N}$ )	$195 \pm 6.3$	24.4 (14%)
Black Carbon ( $\text{Gg C}$ )	$126 \pm 6.5$	76 (140%)
Sulfate ( $\text{Gg S}$ )	$572 \pm 16.5$	369 (206%)
Organic Carbon ( $\text{Gg C}$ )	$1776 \pm 66$	506 (40%)
Dust ( $\text{Tg}$ )	$15.0 \pm 0.56$	-0.21 (-1.6%)
Sea Salt ( $\text{Tg}$ )	$6.35 \pm 0.10$	-0.06 (-1.0%)

## Figures

Figure 1. Change in annual mean surface emissions from 1860 to 2000 for nitrogen oxide (NO), carbon monoxide (CO), non-methane volatile organic compounds (NMVOCs), black carbon (BC), organic carbon (OC), and sulfur dioxide (SO<sub>2</sub>). Surface emissions include emissions from anthropogenic sources, biomass burning, and ships.

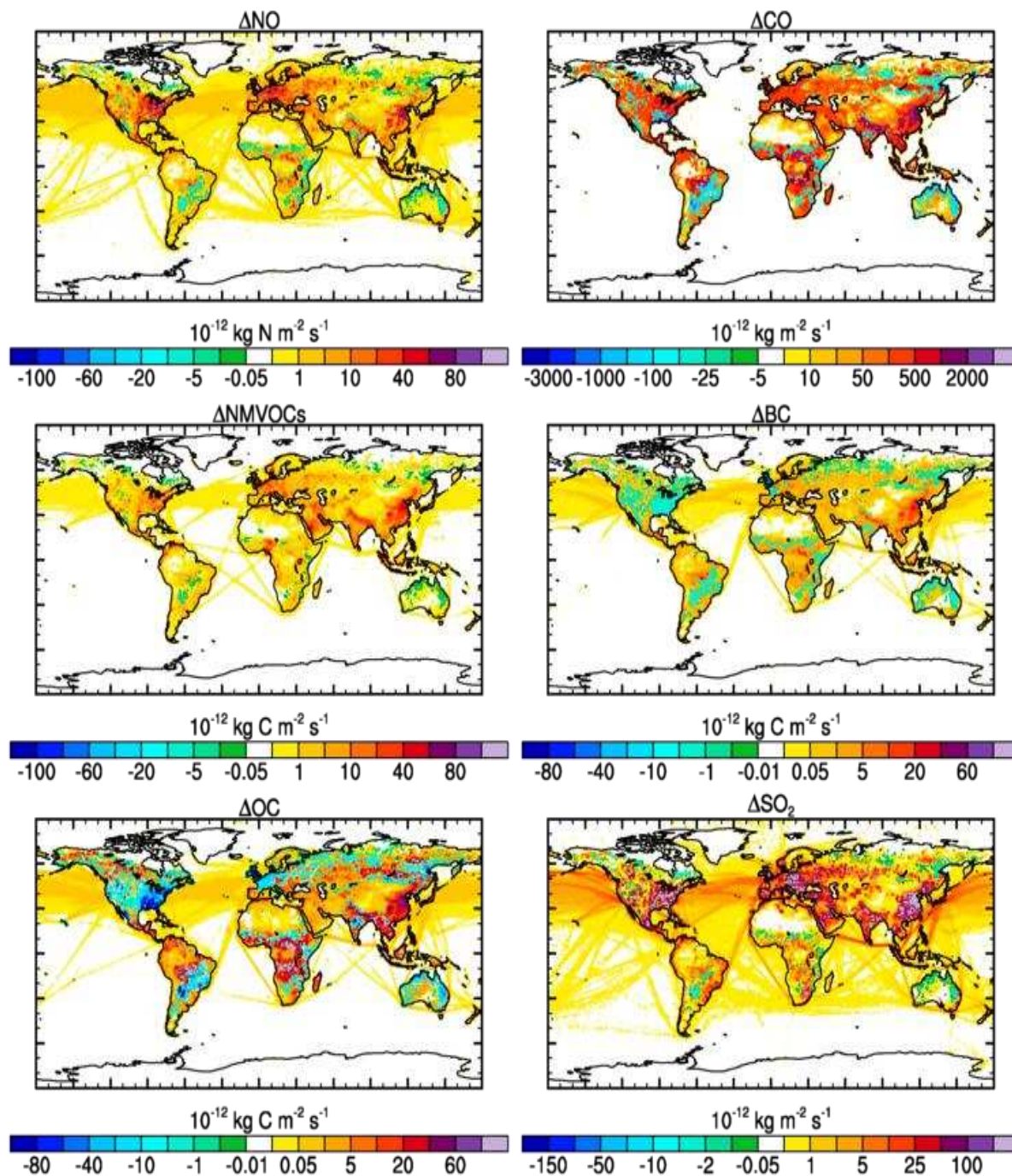


Figure 2. Comparison of simulated monthly mean ozone (ppbv) with observed ozonesonde climatology for the period 1995 to 2009 at vertical levels of 800 (left), 500 (center) and 200 hPa (right). Monthly mean ozonesonde observations are shown in black dots. Vertical lines indicate standard deviation over the 1995-2009 time period. Model ozone is averaged for 1981-2000 (red) and 1995-2007 (blue) time periods.

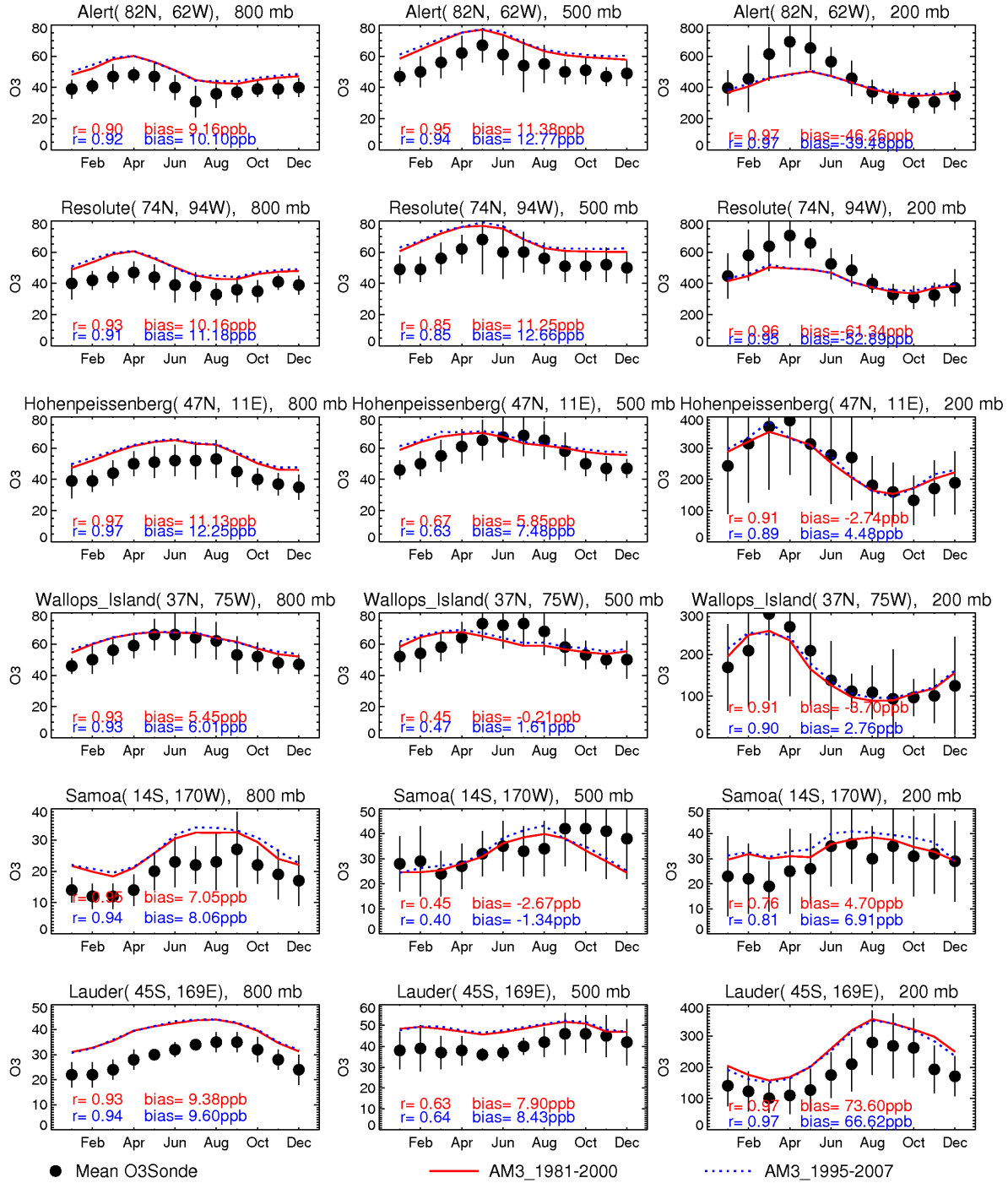


Figure 3. Zonal annual mean absolute bias of AM3 a)  $O_3$  and b) CO concentration relative to measurements by the Tropospheric Emission Spectrometer (TES) aboard the Aura satellite for the period 2005 to 2007. Bias is calculated as AM3 minus TES in units of ppbv.

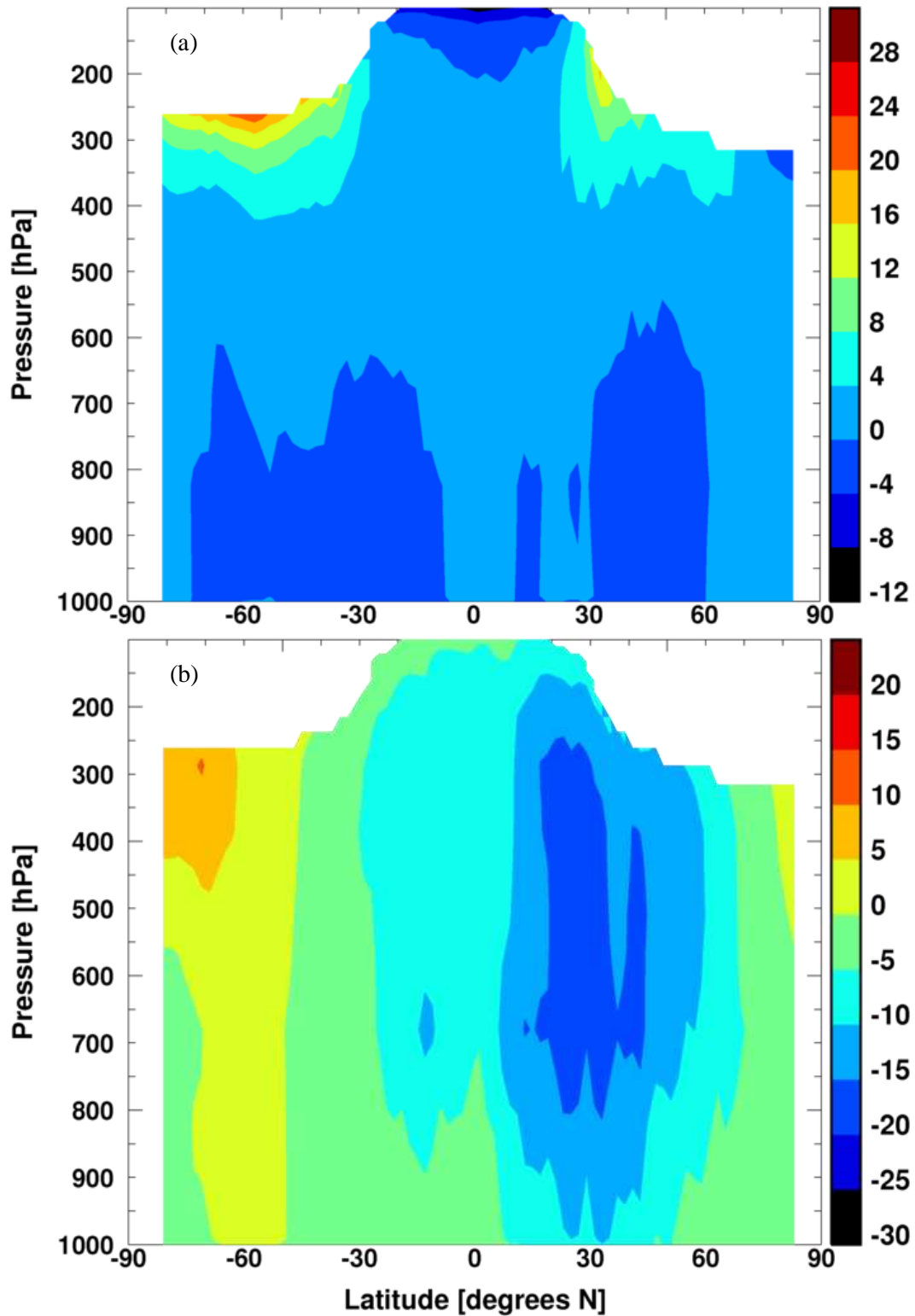


Figure 4. Comparison of AM3 simulated monthly mean surface ozone (ppbv) for 1981-2000 with measurements from CASTNet (<http://www.epa.gov/castnet/>) in the United States (1988-2009), EMEP (<http://www.nilu.no/projects/ccc/emepdata.html>) in Europe (1987-2008), and three sites in India. Black and red lines show the monthly mean observed and simulated surface ozone concentrations, respectively, averaged over all the sites falling within each region (defined in Table S1). Grey lines show ozone concentrations observed at each site included in the region. Vertical black lines denote standard deviation in observed concentrations across the sites. For the Indian sites, vertical lines represent standard deviation in measurements.

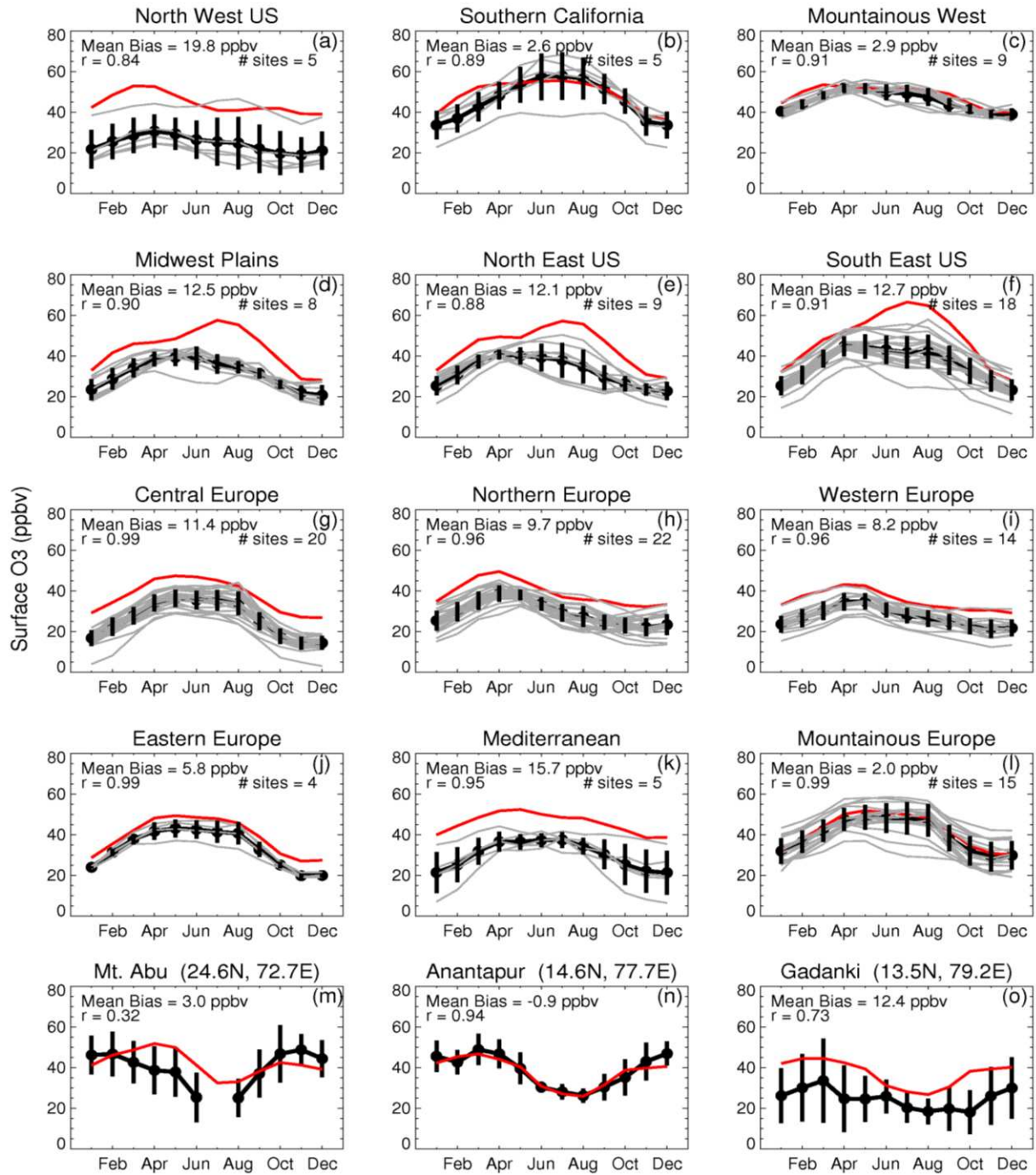


Figure 5. Comparison of model simulated monthly mean (red line) with observed CO concentrations (black dots) at surface sites. Observations are from Novelli and Masarie (2010) for the 1988 to 2010. Vertical lines represent the standard deviations of the observations within a month.

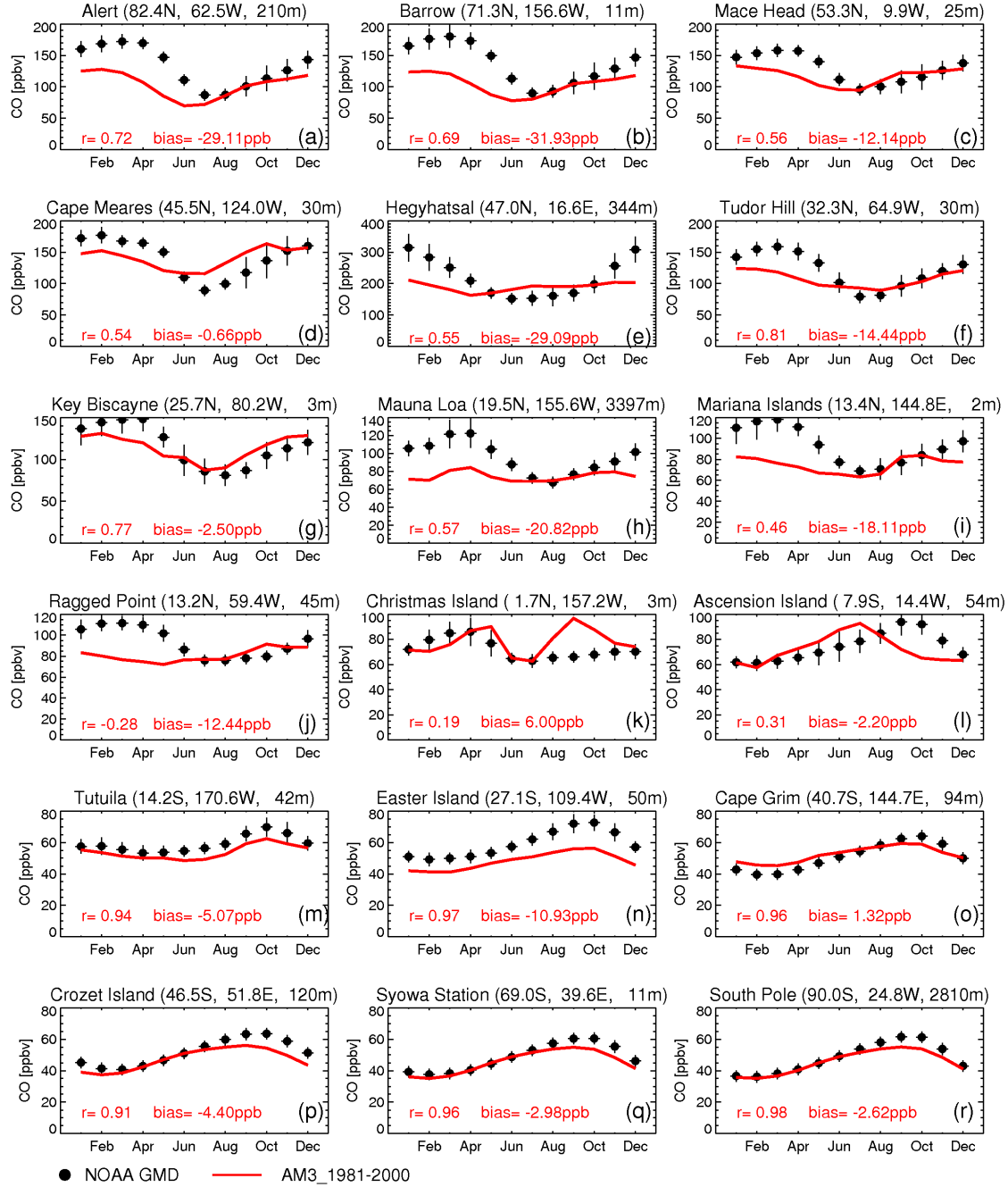


Figure 6. Evolution of the global oceanic annual mean aerosol optical depth at 550 nm retrieved from AVHRR, and that simulated by AM3 with tropospheric aerosols (dashed line), and both tropospheric and volcanic aerosols (dash-dotted line) from 1982 to 2006 (top panel), and spatial distribution of annual mean oceanic aerosol optical depth at 550 nm averaged over 1996 to 2006 time period simulated by AM3 (bottom left, tropospheric aerosols only) and that retrieved from AVHRR (bottom right). Global and oceanic mean AOD simulated by AM3 is indicated on the left and right, respectively, and oceanic mean AOD observed by AVHRR is shown on the right on the bottom panels.

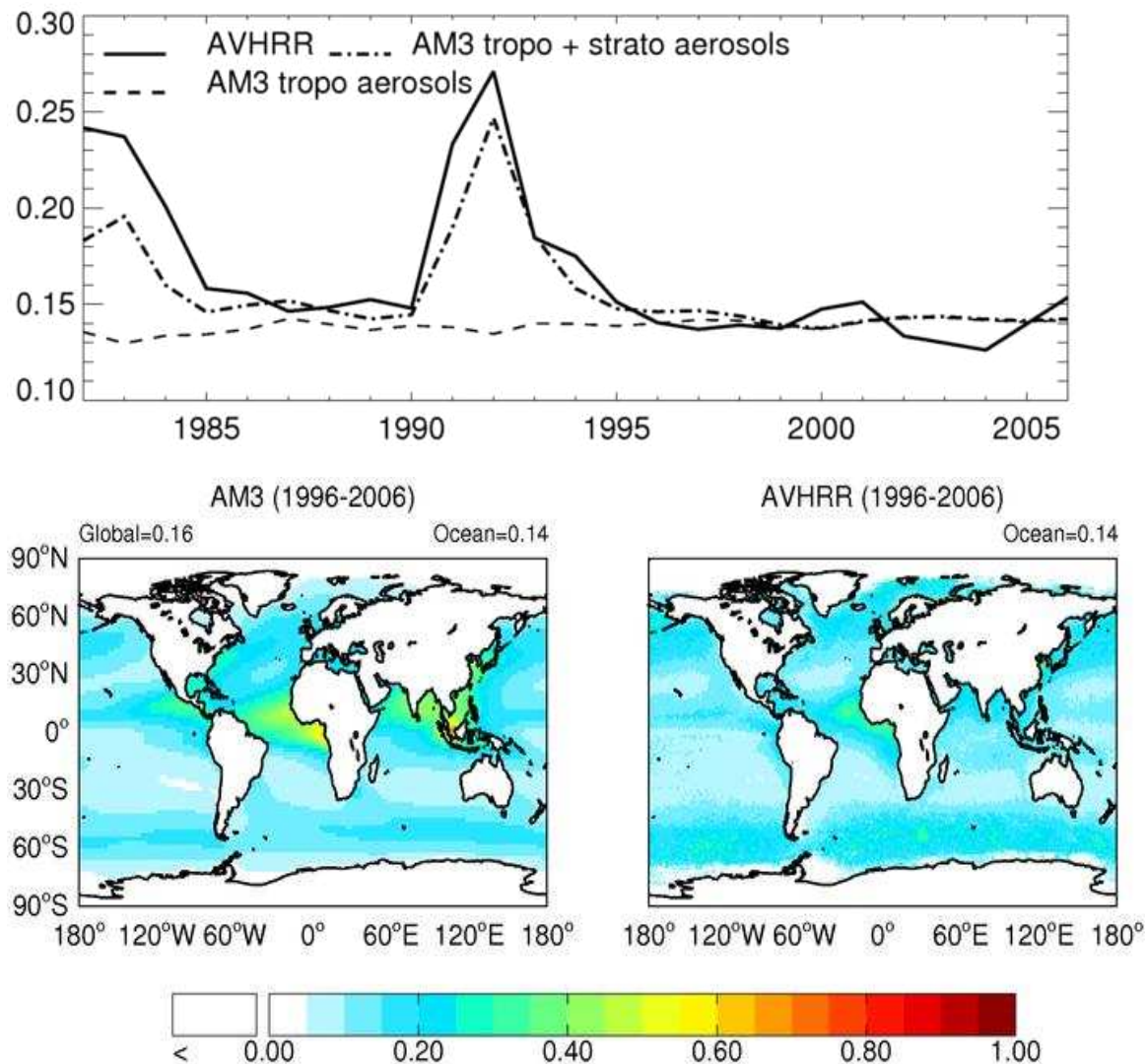


Figure 7. (a) Annual mean OH burden from AM3 compared with the (b) climatological mean of Spivakovsky et al. [2000], (c) percent change in airmass-weighted mean OH concentrations in various subdomains of the atmosphere and (d) ratio of present day (2000) to preindustrial (1860) mean OH in the surface to 750 hPa subdomain of the atmosphere.

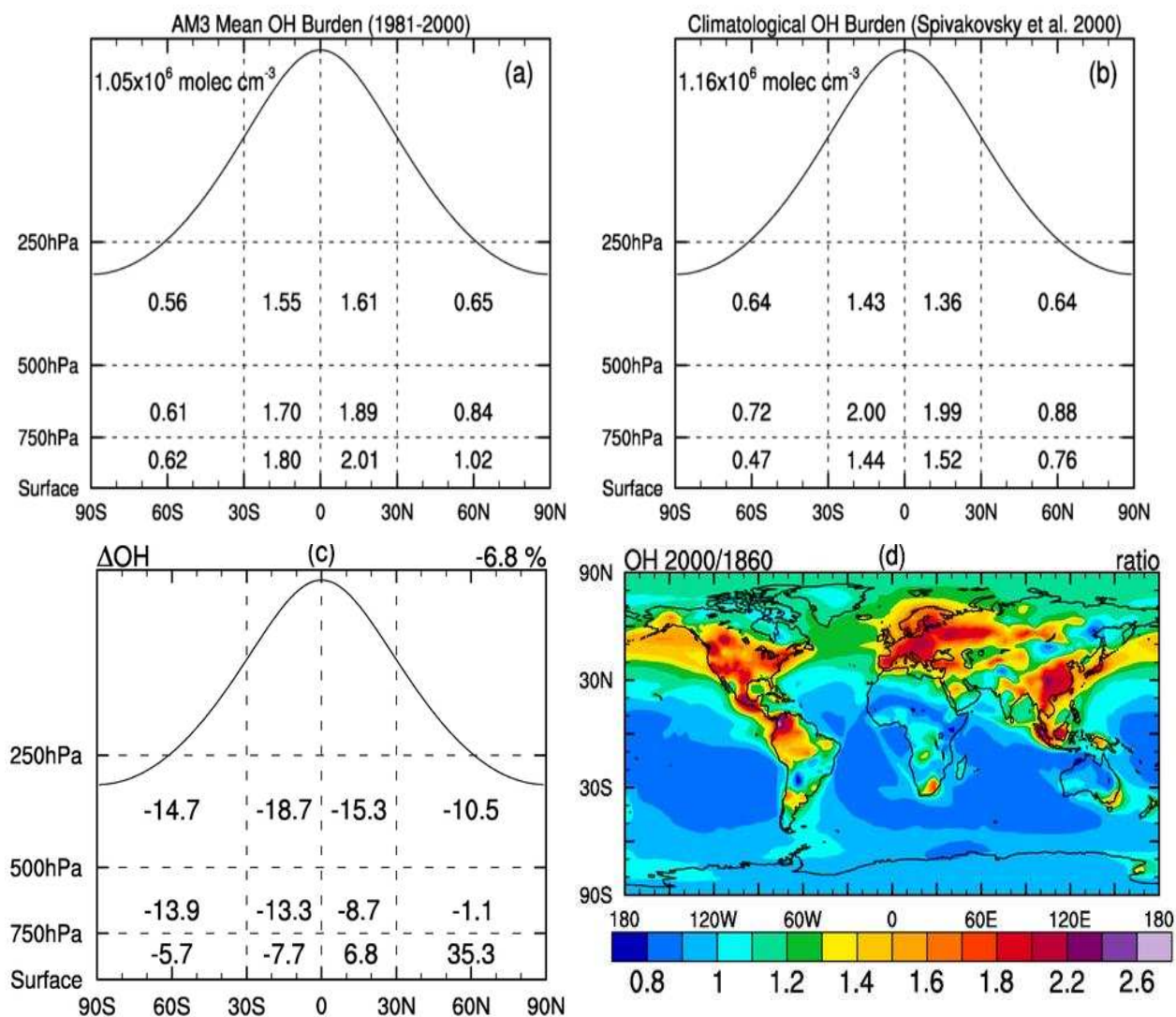


Figure 8. AM3 simulated changes in column burden (left panel) and surface (right panel) concentrations of a, b)  $O_3$ , c, d)  $CO$ , e, f) tropospheric  $NO_x$ , g, h) sulfate ( $SO_4^-$ ), i, j) black carbon (BC), and l, k) organic carbon (OC) in response to short-lived pollutant emission changes from preindustrial to present day (2000-1860). Units for each variable plotted are shown on top right corner. Areas where change is insignificant ( $p=95\%$  student's t-test) are not colored.

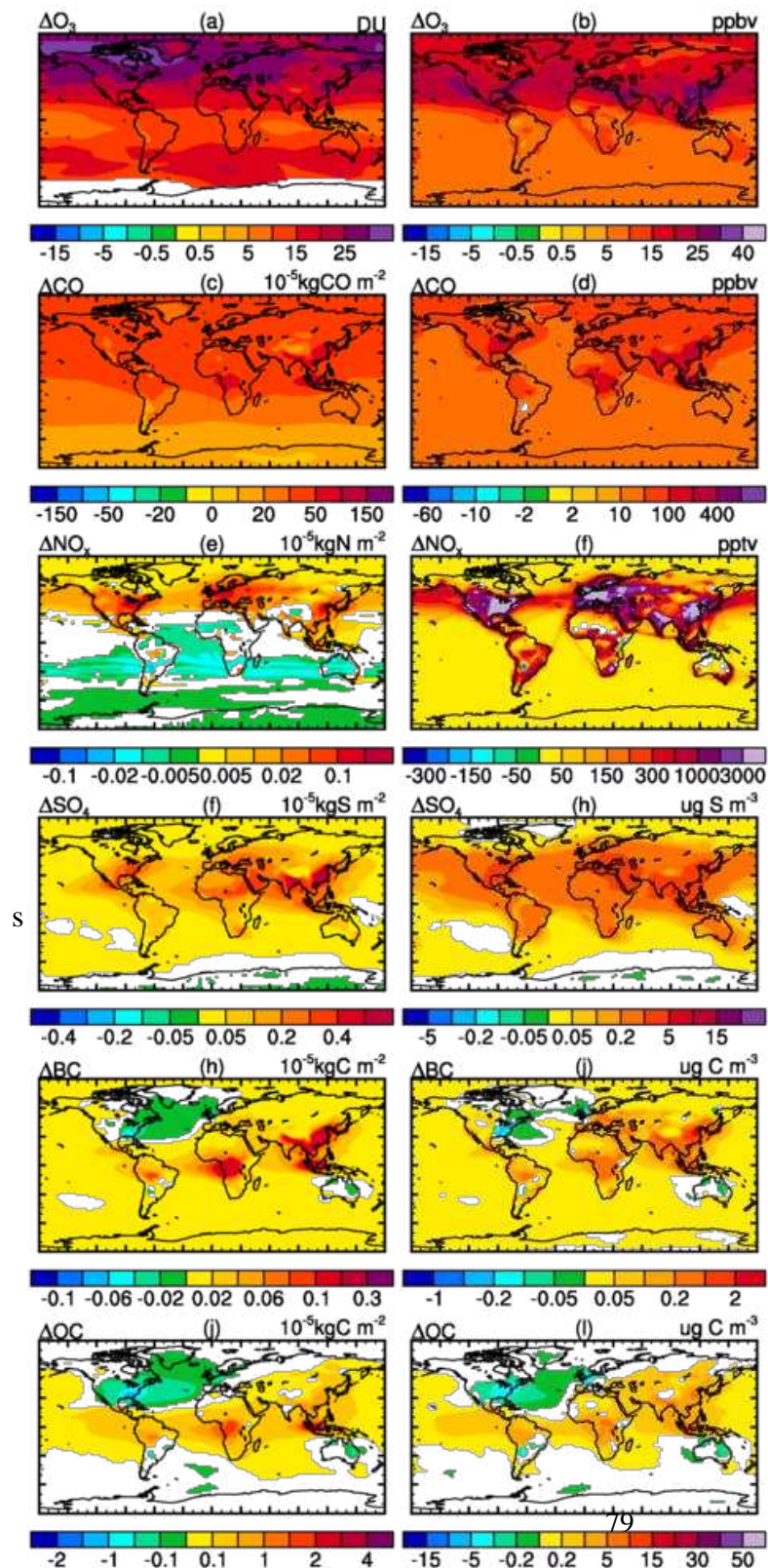


Figure 9. (a) Contribution of each aerosol species simulated by AM3 to the global annual mean AOD for present day (2000) and preindustrial (1860) and (b) preindustrial to present day change in annual mean aerosol optical depth (AOD) at 550 nm; global mean value is indicated on top right of the plot.

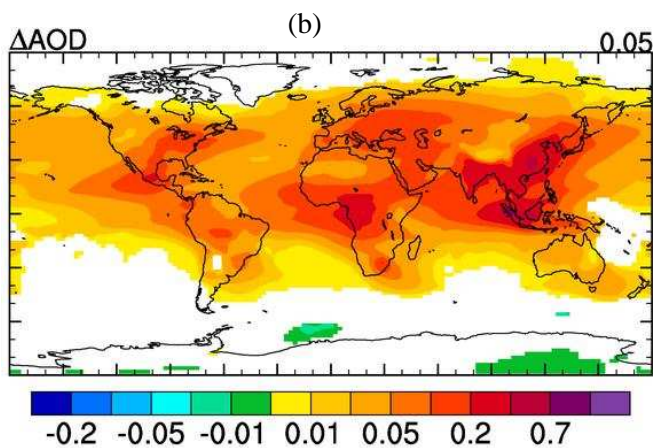
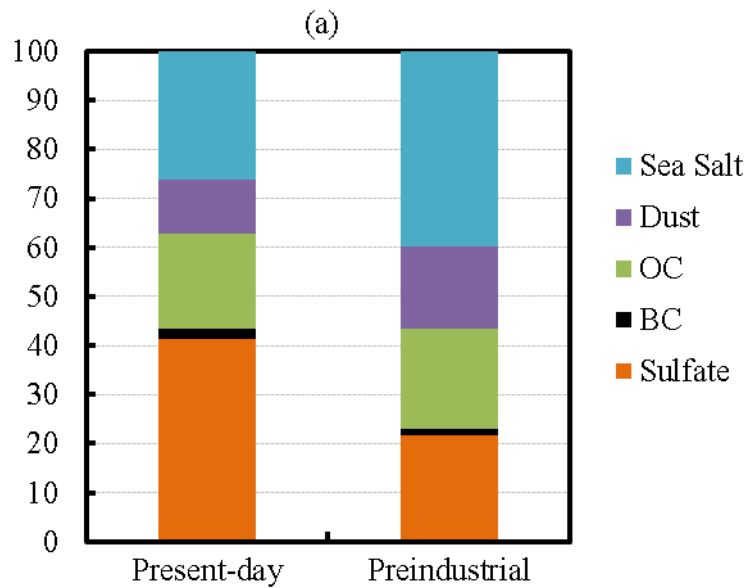


Figure 10. Net annual mean top-of-the-atmosphere a) all-sky radiative perturbation flux (RFP), b) clear-sky RFP, and c) cloudy-sky RFP, due to changes in short-lived pollutant emissions from preindustrial to present day. Global mean values are indicated at top right of each plot. Areas where change is insignificant ( $p=95\%$  student's t-test) are not colored.

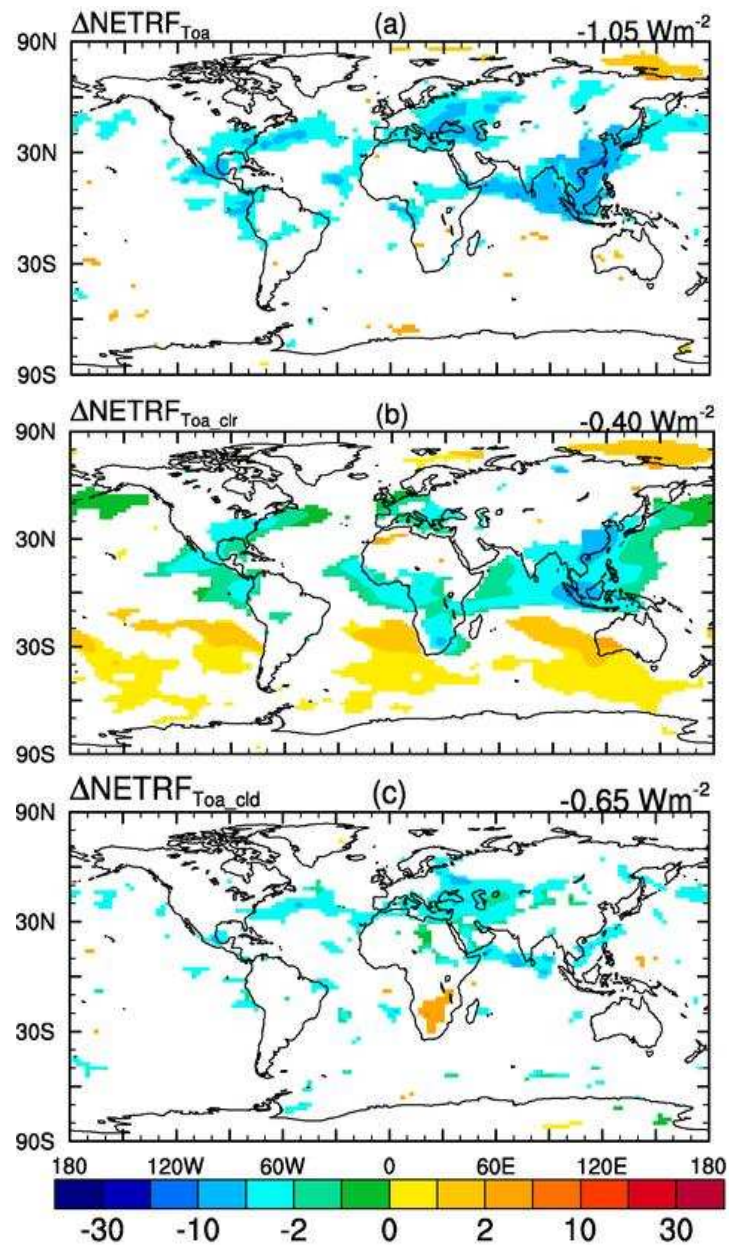
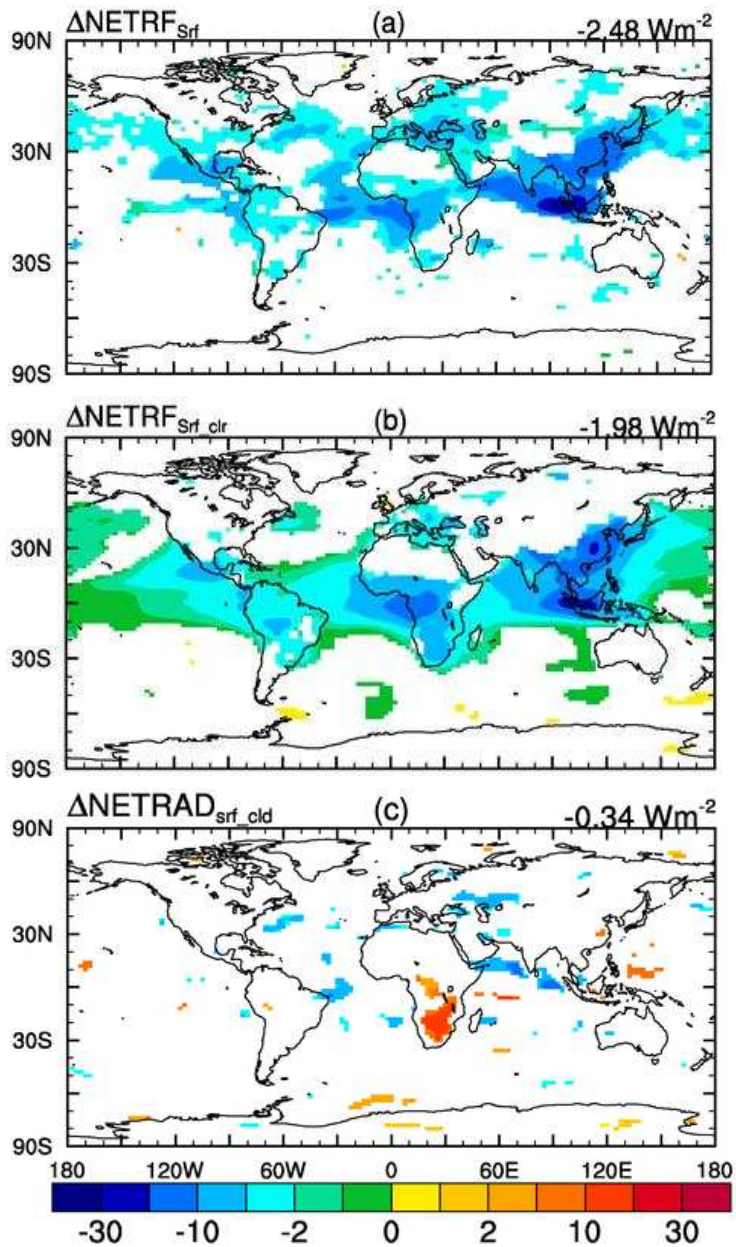


Figure 11. Net annual mean surface a) all-sky radiative perturbation flux (RFP), b) clear-sky RFP, and c) cloudy-sky RFP, due to changes in short-lived pollutant emissions from preindustrial to present day. Global mean values are indicated at top right of each plot. Areas where change is insignificant ( $p=95\%$  student's  $t$ -test) are not colored.



## Supplementary Information

### Preindustrial to Present day Impact of Short-lived Pollutant Emissions on Atmospheric Composition and Climate Forcing

Vaishali Naik<sup>1\*</sup>, Larry W. Horowitz<sup>2</sup>, Arlene M. Fiore<sup>3</sup>, Paul Ginoux<sup>2</sup>, Jingqiu Mao<sup>4</sup>, Adetutu M. Aghedo<sup>5</sup>, and Hiram Levy II<sup>2</sup>

<sup>1</sup> UCAR/NOAA Geophysical Fluid Dynamics Laboratory, Princeton, New Jersey.

<sup>2</sup> NOAA Geophysical Fluid Dynamics Laboratory, Princeton, New Jersey.

<sup>3</sup> Department of Earth and Environmental Sciences and Lamont-Doherty Earth-Observatory, Columbia University, Palisades, New York, New York.

<sup>4</sup> Atmospheric and Oceanic Sciences, Princeton University, Princeton, New Jersey.

<sup>5</sup> Civil and Environmental Engineering, Rice University, Houston, Texas.

\* **Corresponding Author:** [Vaishali.Naik@noaa.gov](mailto:Vaishali.Naik@noaa.gov)

Table S1. Geographical location of stations with surface ozone observations considered for evaluation of the seasonal cycle of surface O<sub>3</sub> from GFDL-AM3.

<b>Region</b>	<b>Station</b>	<b>State/ Country</b>	<b>Longitude (°E)</b>	<b>Latitude (°N)</b>	<b>Altitude (masl)</b>
<b>North West US</b>	North Cascades NP	WA	-121.4	48.5	109.0
	Olympic NP	WA	-123.4	48.1	125.0
	Mount Rainier NP	WA	-122.1	46.8	415.0
	Glacier NP	MT	-114.0	48.5	976.0
	Lassen Volcanic NP	CA	-121.6	40.5	1756.0
<b>Southern California</b>	Death Valley NM	CA	-116.8	36.5	125.0
	Pinnacles NM	CA	-121.2	36.5	335.0
	Sequoia NP - Lookout Pt	CA	-118.8	36.4	1225.0
	Joshua Tree NM	CA	-116.4	34.1	1244.0
	Yosemite NP - Turtleback Dome	CA	-119.7	37.7	1605.0
<b>Mountainous West US</b>	Gothic	CO	-107.0	39.0	2926.0
	Great Basin NP	NV	-114.2	39.0	2060.0
	Mesa Verde NP	CO	-108.5	37.2	2165.0
	Pinedale	WY	-109.8	42.9	2388.0
	Rocky Mtn NP	CO	-105.5	40.3	2743.0
	Yellowstone NP	WY	-110.4	44.6	2400.0
	Grand Canyon NP	AZ	-112.2	36.1	2073.0
	Canyonlands NP	UT	-109.8	38.5	1809.0
	Chiricahua NM	AZ	-109.4	32.0	1570.0
<b>Midwest Plains US</b>	Caddo Valley	AR	-93.1	34.2	71.0
	Stockton	IL	-90.0	42.3	274.0
	Theodore Roosevelt NP	ND	-103.4	46.9	850.0
	Voyageurs NP	MN	-92.8	48.4	429.0
	Alhambra	IL	-89.6	38.9	164.0
	Bondville	IL	-88.4	40.1	212.0
	Perkinstown	WI	-90.6	45.2	472.0
	Vincennes	IN	-87.5	38.7	134.0
<b>North East US</b>	Wash. Crossing	NJ	-74.9	40.3	61.0
	Arendtsville	PA	-77.3	39.9	269.0
	Penn State	PA	-77.9	40.7	378.0
	Connecticut Hill	NY	-76.7	42.4	501.0
	Abington	CT	-72.0	41.8	209.0
	Woodstock	NH	-71.7	43.9	258.0

	Acadia NP	ME	-68.3	44.4	158.0
	Ashland	ME	-68.4	46.6	235.0
	Howland	ME	-68.7	45.2	69.0
<b>South East US</b>	Beltsville	MD	-76.8	39.0	46.0
	Blackwater NWR	MD	-76.1	38.4	4.0
	Horton Station	VA	-80.6	37.3	920.0
	Prince Edward	VA	-78.3	37.2	150.0
	Shenandoah NP - Big Meadows	VA	-78.4	38.5	1073.0
	Cadiz	KY	-87.8	36.8	189.0
	Crockett	KY	-83.1	37.9	455.0
	Mackville	KY	-85.0	37.7	353.0
	Edgar Evins	TN	-85.7	36.0	302.0
	Great Smoky NP - Look Rock	TN	-83.9	35.6	793.0
	Speedwell	TN	-83.8	36.5	361.0
	Coweeta	NC	-83.4	35.1	686.0
	Cranberry	NC	-82.0	36.1	1219.0
	Beaufort	NC	-76.6	34.9	2.0
	Candor	NC	-79.8	35.3	198.0
	Sand Mountain	AL	-86.0	34.3	352.0
	Coffeeville	MS	-89.8	34.0	134.0
	Georgia Station	GA	-84.4	33.2	270.0
<b>Central Europe</b>	Illmitz	AT	16.8	47.8	117.0
	Heidenreichstein	AT	15.0	48.9	570.0
	Dunkelsteinerwald	AT	15.5	48.4	320.0
	Gänserndorf	AT	16.7	48.3	161.0
	Stixneusiedl	AT	16.7	48.1	240.0
	Offagne	BE	5.2	49.9	430.0
	Eupen	BE	6.0	50.6	295.0
	Vezin	BE	5.0	50.5	160.0
	Payerne	CH	6.9	46.8	510.0
	Tänikon	CH	8.9	47.5	540.0
	Sion	CH	7.3	46.2	480.0
	Langenbrügge	DE	10.8	52.8	74.0
	Deuselbach	DE	7.1	49.8	480.0
	Neuglobsow	DE	13.0	53.2	62.0
	Bassum	DE	8.7	52.8	52.0
	Ansbach	DE	10.6	49.2	481.0
	Ueckermünde	DE	14.1	53.8	1.0
	Lückendorf	DE	14.8	50.8	490.0

	Kollumerwaard	NL	6.3	53.3	1.0
	Vredepeel	NL	5.9	51.5	28.0
<b>Northern Europe</b>	Ulborg	DK	8.4	56.3	10.0
	Frederiksborg	DK	12.3	56.0	10.0
	Lille Valby	DK	12.1	55.7	10.0
	Utö	FI	21.4	59.8	7.0
	Virolahti II	FI	27.7	60.5	4.0
	Oulanka	FI	29.4	66.3	310.0
	Birkenes	NO	8.2	58.4	190.0
	Tustervatn	NO	13.9	65.8	439.0
	Jergul	NO	24.6	69.4	255.0
	Kårvatn	NO	8.9	62.8	210.0
	Osen	NO	11.8	61.2	440.0
	Prestebakke	NO	11.5	59.0	160.0
	Nordmoen	NO	11.1	60.3	200.0
	Jeløya	NO	10.6	59.4	5.0
	Voss	NO	6.5	60.6	500.0
	Valle	NO	7.6	59.0	250.0
	Rörvik	SE	11.9	57.4	10.0
	Vavihill	SE	13.1	56.0	175.0
	Aspvreten	SE	17.4	58.8	20.0
	Esrang	SE	21.1	67.9	475.0
	Norra-Kvill	SE	15.6	57.8	261.0
	Vindeln	SE	19.8	64.2	225.0
<b>Western Europe</b>	Eskdalemuir	GB	-176.8	55.3	243.0
	Lough Navar	GB	-172.1	54.4	126.0
	Yarner Wood	GB	-176.3	50.6	119.0
	High Muffles	GB	-179.2	54.3	267.0
	Strath Vaich Dam	GB	-175.2	57.7	270.0
	Aston Hill	GB	-177.0	52.5	370.0
	Bottesford	GB	-179.2	52.9	32.0
	Bush	GB	-176.8	55.9	180.0
	Glazebury	GB	-177.5	53.5	21.0
	Harwell	GB	-178.7	51.6	137.0
	Ladybower Res.	GB	-178.2	53.4	420.0
	Lullington Heath	GB	0.2	50.8	120.0
	Sibton	GB	1.5	52.3	46.0
	Wharleycroft	GB	-177.5	54.6	206.0
<b>Eastern Europe</b>	Svratouch	CZ	16.0	49.7	737.0
	Kosetice	CZ	15.1	49.6	534.0

	Preila	LT	21.1	55.3	5.0
	Kovk	SI	15.1	46.1	600.0
	Mediterranean				
	Roquetas	ES	0.5	40.8	44.0
	Logroño	ES	-177.5	42.5	445.0
	Noya	ES	-171.1	42.7	683.0
	Ispra	IT	8.6	45.8	209.0
	Monte Velho	PT	-171.2	38.1	43.0
<b>Mountainous Europe</b>	St. Koloman	AT	13.2	47.7	851.0
	Sulzberg	AT	9.9	47.5	1020.0
	Stolzalpe bei Murau	AT	14.2	47.1	1302.0
	Sonnblick	AT	13.0	47.1	3106.0
	Zillertaler Alpen	AT	11.9	47.1	1970.0
	Gerlitzten	AT	13.9	46.7	1895.0
	Haunsberg	AT	13.0	48.0	730.0
	Schauinsland	DE	7.9	47.9	1205.0
	Brotjacklriegel	DE	13.2	48.8	1016.0
	Schmücke	DE	10.8	50.7	937.0
	San Pablo de los Montes	ES	-175.7	39.5	917.0
	Great Dun Fell	GB	-177.6	54.7	847.0
	Zarodnje	SI	15.0	46.4	770.0
	Krvavec	SI	14.5	46.3	1740.0
	Stará Lesná	SK	20.3	49.2	808.0
<b>India</b>	Mt. Abu	Rajasthan	72.7	24.6	1680.0
	Anantapur	Andhra Pradesh	77.6	14.6	331.0
	Gadanki	Tamil Nadu	79.2	13.5	340.0

Figure S1. AM3 simulated annual mean surface ozone concentrations for a) preindustrial and b) present-day. Global average surface ozone concentrations are shown at the upper right corner of each plot.

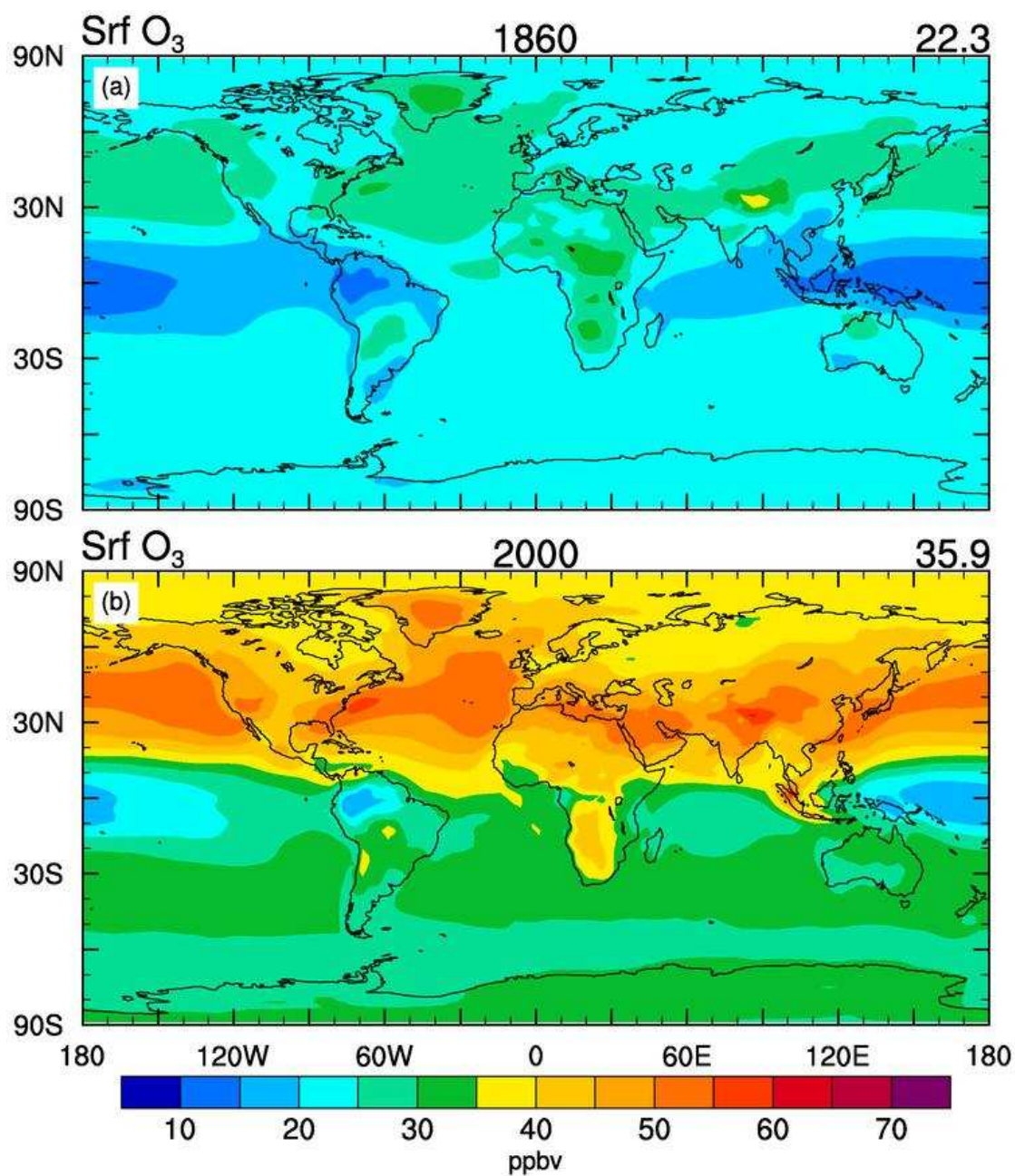


Figure S2. AM3 simulated change in annual mean lightning  $\text{NO}_x$  emissions and flash frequency in response to short-lived pollutant changes from preindustrial to present day (2000 – 1860).

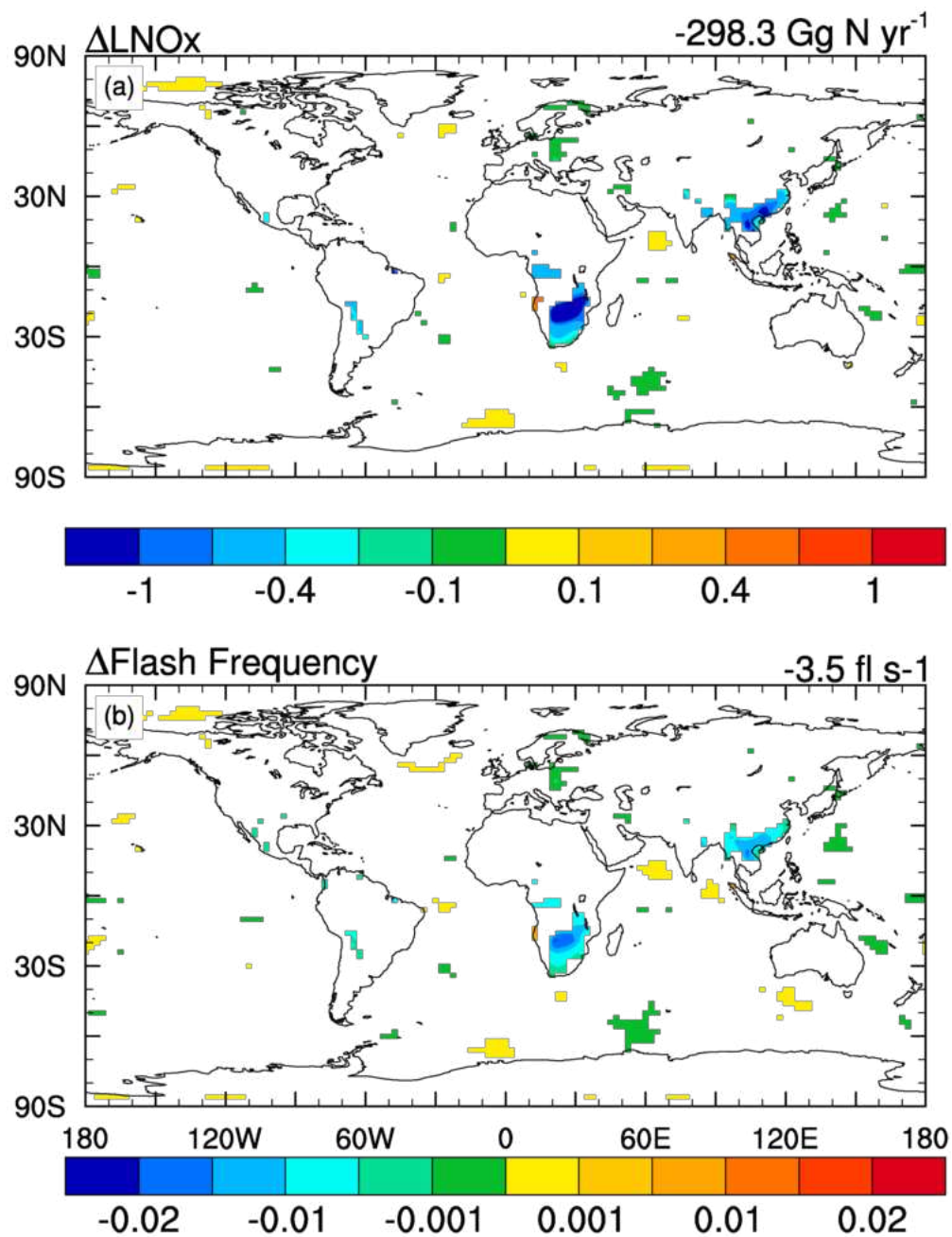


Figure S3. AM3 simulated change in annual mean a) air temperature at 2-m height (K), b) precipitation ( $\text{mm day}^{-1}$ ), c) total cloud cover (%) and d) liquid water path in response to short-lived pollutant changes from preindustrial to present day (2000 – 1860). Areas where change is insignificant ( $p=95\%$  student's t-test) are not colored. Global mean changes are indicated at top-right corner of each plot.

